TAMPEREEN TEKNILLINEN YLIOPISTO
TAMPERE UNIVERSITY OF TECHNOLOGY

MIKKO FOLKERSMA

LARGE EDDY SIMULATION OF AN ASYMMETRIC JET IN CROSSFLOW

Master of Science thesis

Examiner: Prof. Hannu Ahlstedt
Examiner and topic approved by the
Faculty Council of the Faculty of
Engineering Sciences
on 8 April 2015

ABSTRACT

MIKKO FOLKERSMA: Large Eddy Simulation of an Asymmetric Jet in Crossflow
Tampere University of Technology
Master of Science thesis, 54 pages, 2 Appendix pages
October 2015
Master's Degree Programme in Mechanical Engineering
Major: Fluid Dynamics
Examiner: Prof. Hannu Ahlstedt
Keywords: CFD, LES, jet in crossflow, entrainment, turbulent scalar flux

A high fidelity large eddy simulation (LES) of an asymmetric jet in crossflow is performed to study passive scalar mixing. The configuration includes the most relevant physics of a film cooling application. The simulation is validated with an experiment which has exactly the same geometry.

The compound angle injection leads to an asymmetric counter-rotating vortex pair (CVP) in which one vortex dominates the other. This CVP is highly responsible for the shape of the jet in the far field. The entrainment of the present jet is calculated and compared with a symmetric jet without a compound angle.

The evolution of the turbulent scalar flux is studied by analysing its transport equations. The production term is closely examined because its shape resembles the turbulent scalar flux. In addition, the commonly used algebraic models in Reynolds-averaged Navier-Stokes (RANS) exploit it. The algebraic models are evaluated and the applicability of the models is further discussed.

TIIVISTELMÄ

MIKKO FOLKERSMA: Epäsymmetrisen ristivirtaussuihkun mallintaminen suurten pyörteiden simuloinnilla
Tampereen teknillinen yliopisto
Diplomityö, 54 sivua, 2 liitesivua
Lokakuu 2015
Konetekniikan koulutusohjelma
Pääaine: Virtaustekniikka
Tarkastaja: Prof. Hannu Ahlstedt
Avainsanat: CFD, LES, ristivirtaussuihku, turbulentti skalaarivirta

Tässä työssä tutkitaan passiivisen skalaarin sekoittumista epäsymmetrisessä ristivirtaussuihkussa suurten pyörteiden simuloinnilla (LES). Laskentamalli kuvaa yksinkertaistettua kalvolauhtumisprosessia. Simulointi validoidaan käyttäen mittausdataa samanlaisesta geometriasta.

Kallistettu ja käännetty suihku johtaa epäsymmetriseen vastakkain pyörivään pyörreparii (CVP), jossa toinen pyörre on voimakkaampi kuin toinen. Voimakkaampi pyörre on vastuussa suihkun poikkileikkauksen muodosta kaukana suihkun injektioreiästä. Epäsymmetrisen ristivirtaussuihkun sekoittumista verrataan symmetriseen ristivirtaussuihkuun, jota ei ole käännetty virtaussuuntaan nähden.

Turbulentin skalaarivirran kehittymistä analysoidaan tutkimalla sen kuljettumisyhtälöä. Erityisesti tuottotermiin keskitytään, koska sen muoto muistuttaa itse turbulenttia skalaarivirtaa ja tuottotermiä käytetään hyväksi turbulentin skalaarivirran mallintamiseen yleisimmissä algebrallisissa Reynoldsin yhtälöjärjestelmän sulkeumissa. Yleisimpien algebrallisten mallien soveltuvuutta arvioidaan vertaamalla niistä saatuja tuloksia tämän työn simulointituloksiin.

PREFACE

This work was done in ISAE SUPAERO in Toulouse, France. I gratefully acknowledge the financial support from Honeywell and the computational resources from Calmip (EOS) and IDRIS (Turing).

First and foremost I would like to thank my supervisor Assistant Professor Julien Bodart for his help and advice during the project. I would also like to thank all the personnel of DAEP for the opportunity and great experience in Toulouse. Additionally, I am grateful to the examiner Professor Hannu Ahlstedt.

I admire the developers of Paraview, matplotlib and Numpy for their great free and open-source software which I used extensively throughout the work.

Last but not least I want to thank my fiancée Aino Saari for her encouragements, patience and support during the work.

Tampere, September 2015

Mikko Folkersma

TABLE OF CONTENTS

LIST OF ABBREVIATIONS AND SYMBOLS

Abbreviations

CFD	Computational Fluid Dynamics
CFL	Courant-Friedrichs-Levy
CPU	Central Processing Unit
CVP	Counter-Rotating Vortex Pair
DNS	Direct Numerical Simulation
SGDH	Standard Gradient Diffusion Hypothesis
GGDH	Generalized Gradient Diffusion Hypothesis
GB	Gigabyte
HOGGDH	High-Order Gradient Diffusion Hypothesis
FLOPS	Floating-point Operations Per Second
LES	Large Eddy Simulation
MRI	Magnetic Resonance Image
PIV	Particle Image Velocimetry
MPI	Message Passing Library
RAM	Random-Access Memory
RANS	Reynolds-Averaged Navier-Stokes
SGS	Subgrid-Scale
TB	Terabyte

Symbols

A	Advection of the turbulent scalar flux
C	Constant
C	Mean passive scalar concentration
c	Passive scalar concentration
c	Heat capacity
c	Speed of the sound
D	Dissipation of the turbulent scalar flux
D	Jet hole diameter
$\mathcal{D}$	Mass diffusivity
E	Total energy
h	Heat transfer coefficient
I	Momentum ratio
k	Turbulence kinetic energy

L	Characteristic length
l	Length scale
P	Production of the turbulent scalar flux
Pr	Prandtl number
p	Pressure
Q	Q-criterion
q	Heat flux
q	Filtered scalar flux
Re	Reynolds number
R	Specific gas constant
r	Velocity ratio
S	Rate-of-strain tensor
Sc	Schmidt number
T	Temperature
T	Transport of the turbulent scalar flux
t	Time
U	Mean velocity
U_τ	Friction velocity
u	Velocity
$\overline{u_i' c'}$	Turbulent scalar flux
x, y, z	Coordinates axes
x^+, y^+, z^+	Wall distances
α	Thermal diffusivity
Δ	Cell size
δ	Boundary layer thickness
ϵ	Dissipation rate of turbulence kinetic energy
η	Cooling efficiency
θ	Compound angle
θ	Momentum thickness
κ	Wavenumber
μ	Dynamic viscosity
ν	Kinematic viscosity
ρ	Density
σ	Viscous stress
τ	Filtered momentum field
τ	Time scale
Φ	Pressure scrambling of the turbulent scalar flux
ϕ, φ	Dummy variables
φ	Injection angle
ω	Vorticity

1. INTRODUCTION

Efficient fuel usage is crucial in aircrafts regarding economical and environmental considerations. In the process of converting fuel energy to thrust the ratio of fuel consumed to get the required thrust should be minimized. Common types of aircraft engines use a gas turbine of which the efficiency can be improved by increasing the operating temperature. The temperature of the hot gas which is entering to the gas turbine's turbine is directly proportional to the efficiency. Consequently, in modern high performance gas turbines the temperature may exceed the melting point of the turbine's blade material and therefore the blade has to be cooled down. A common approach to the problem is film cooling in which relatively cool jets are ejected from the surface of the blade (Figure 1.1(a)). With this technique, the jet forms a thin layer of coolant which protects the blade. This film cooling approach belongs to the jet in crossflow class of problems which has been under heavy research for decades.

Jet in crossflow refers to a flow configuration in which a jet is discharged from an orifice to a surrounding crossflow. Figure 1.1(b) shows a schematic of the jet in crossflow. This rather simple configuration yields in a turbulent regime to a very complex flow phenomenon. Moreover, the jet in crossflow contains many design variables that may be tuned to maximize the application efficiency for the desired properties. For example, in film cooling the jet should stay attached to the wall to provide the best thermal protection whereas in some other applications high jet penetration for rapid mixing is desired.

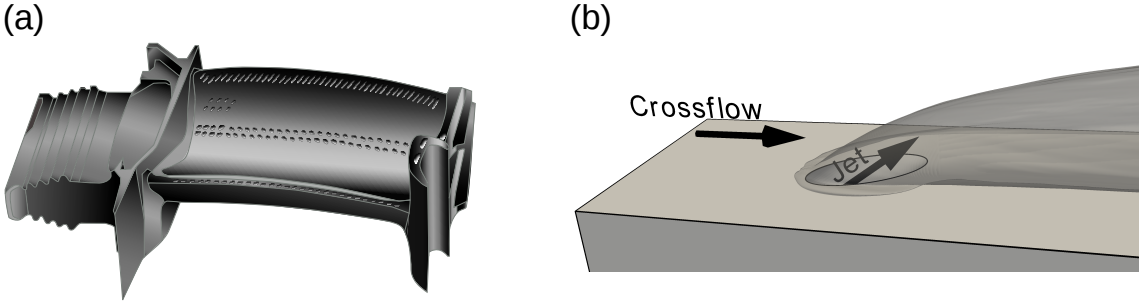

Figure 1.1 *(a) A schematic of a gas turbine blade [41] and (b) a schematic of jet in crossflow configuration.*

In fluid dynamics, turbulence is one of the greatest challenges. Turbulence originates from the instability of the flow which arises when the inertial forces dominate the viscous forces. Reynolds number is a measure of the ratio between these forces. It is given by

$$Re = \frac{\text{inertial forces}}{\text{viscous forces}} = \frac{UL}{\nu}, \tag{1.1}$$

where U is the mean velocity, L is the characteristic length of the problem and ν is the kinematic viscosity. The main characteristic feature of the turbulent flow is chaotic motion which results in fluctuation and enhanced mixing. The chaotic motion includes a wide range of time and length scales. The largest scales are geometry dependent while the smallest scales are bounded by viscosity and therefore a function of the Reynolds number. Consequently, a higher Reynolds number leads to a wider range of length scales.

The system of conservation equations for fluid motion forms the Navier-Stokes equations. Exact analytical solutions for the equations are found only for a few simple flows. For more complex flows, the equations have to be numerically solved using computational fluid dynamics (CFD). CFD is usually divided in three different approaches depending on the level of turbulence modelling. The first approach called direct numerical simulation (DNS) does not use any additional models. The differential equations are solved up to the smallest scale of turbulence and therefore the resulting grid requirements make it computationally very expensive and out of reach for many practical high Reynolds number flows. Consequently, DNS is usually used only for academical purposes and fundamental turbulence understandings. An alternative approach is Reynolds-averaged Navier-Stokes (RANS). In RANS the equations are only solved for the mean flow field and the effect of the fluctuating field which originates from turbulence is modelled. This reduces the computational expense dramatically but the models are usually fine tuned only for specific problems and no universal models exist. Finally, the large eddy simulation (LES) lies between the two previous approaches. In LES the highly geometry dependent large eddies are directly resolved and the more universal small eddies are modelled. LES is particularly suited to intrinsically unsteady problems such as combustion and aeroacoustics as it provides an unsteady description of the flow field because the instantaneous field is solved. Moreover, LES may be used to calibrate the models used in RANS simulations.

The objective of the present work is to run a high fidelity large eddy simulation of a jet in crossflow. The flow configuration represents a simplified film cooling application still relevant to existing industrial systems. The simulation is compared and validated with experiment from the exactly same geometry. The validated

simulation is then used to study the mixing of the jet and the crossflow. Particularly, the evolution of turbulent scalar flux is studied by analysing the transport equation for it. Finally, the applicability of common models used in RANS computations for the turbulent scalar flux is investigated.

2. JET IN CROSSFLOW

This section introduces the jet in crossflow configuration to give the reader appropriate background for the following chapters. Firstly, a short history review of the studies and equipment used in the studies is given. Secondly, the resulting complex flow phenomenon is presented. Finally, the appropriate design variables for film cooling and their optimal values described in the literature are discussed.

2.1 History of jet in crossflow studies

The jet in crossflow has been studied for decades. The first studies were related to the dispersal of smoke. One of the first studies by Bosanquet and Pearson [6] in 1936 determined how the height of a chimney affects the dispersion of smoke and pollution to the surroundings. In this study the jet refers to the smoke that is ejecting from the chimney and the crossflow is the lateral wind outside the chimney. The number of studies and qualitative details has increased since then dramatically. Recent studies have been motivated by the aeronautical field and in particular the reaction control jets used in rockets and missiles, the take-off and landing equipment for the V/STOL aircraft and the dilution and film cooling jets inside the jet engines.

The equipment allowing both computer and experiment simulations used in the jet in crossflow configurations has advanced. The first computational methods was based on the potential flow theory which assumes frictionless and irrotational flow. One of the earliest models was made by Wooler [42] in 1969. Later, the increase in computing power made feasible solving the Navier-Stokes equations numerically. The first RANS computations for the jet in crossflow were made by Chien and Schetz [7] in 1975. These earliest CFD simulations used grids with up to tens of thousands of grid points. Recently, the rapid increase in computation power has allowed LES and even DNS to provide a full instantaneous three-dimensional field by using larger and larger grid size approaching hundreds of millions of grid points.

Similarly the experimental apparatus used in jet in crossflow studies has improved. The hot-wire and laser Doppler anemometers used by Ramsey and Goldstein [29]

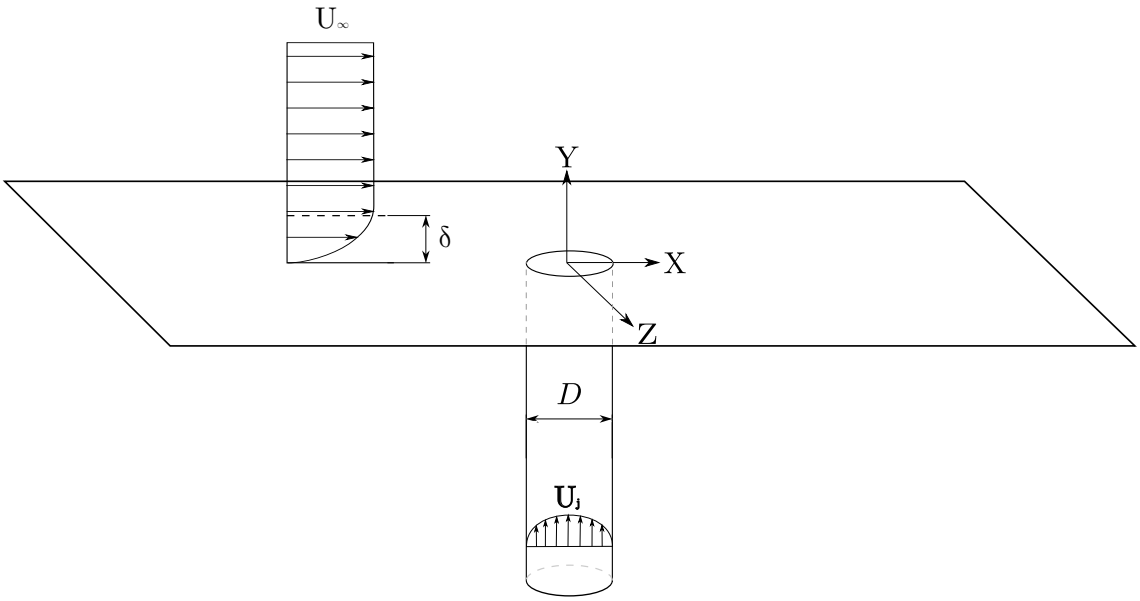

Figure 2.1 *Transverse jet in crossflow configuration. U_∞ is the crossflow velocity, U_{jet} is the jet velocity and δ is boundary layer thickness.*

among the first in 1971 allowed to measure the instantaneous velocity in one direction at one measurement point. An extension to the single-wire probes were the triple-wire probes used by Andreopoulos and Rodi [2] in 1984 and could provide the three-dimensional velocity. Recently, new techniques such as particle image velocimetry (PIV) study by Kuzo [21] in 1996 and magnetic image resonance (MRI) based techniques have allowed to measure the full three dimensional field of velocity and concentration.

2.2 Jet topology

In the jet in crossflow configuration which is given in Figure 2.1 the crossflow flows over a flat plate and encounters the jet which is ejecting from a circular hole perpendicular to the plate. The crossflow induces a boundary layer upstream the interaction with the jet which is either laminar or turbulent depending on the crossflow Reynolds number. The relevant crossflow Reynolds number is defined as

$$Re_\delta = \frac{U_\infty \delta}{\nu}, \tag{2.1}$$

where U_∞ is the crossflow velocity and δ is the boundary layer thickness. The approaching crossflow boundary layer characteristics have a significant effect on the interaction between the jet and crossflow. A thicker crossflow boundary layer thickness means higher jet penetration [25] and higher turbulence level may enhance the mixing of the jet and the crossflow [5].

For the jet inflow most of the simulations use either fully developed laminar or turbulent pipe flow depending on the jet Reynolds number

$$Re_j = \frac{U_{jet}D}{\nu}, \tag{2.2}$$

where U_{jet} is the jet velocity and D is the hole diameter. In film cooling configurations the jet hole is usually short and thus the flow is not fully developed. Consequently, extra caution is required to take the complex jet inflow into account.

An important parameter which characterizes the interaction between the jet and the crossflow is the velocity ratio

$$r = U_{jet}/U_{\infty}. \tag{2.3}$$

The velocity ratio depends on the application. In film cooling the velocity ratio is usually low to keep the jet attached to the wall. In contrast, for dilution jet applications the velocity ratio is high in order to obtain rapid mixing and high jet penetration.

A sketch of the flow topology which results from the interaction between the jet and the crossflow is shown in Figure 2.2. A signature feature is the counter-rotating vortex pair (CVP) which is observed downstream the jet exit hole. The jet shear layer vortices form at the interface of the jet and crossflow on the windward side. The horseshoe vortices form upstream the jet exit hole near the leading edge and the wake vortices form downstream the jet exit hole between the jet and the wall.

The structure of the jet in crossflow is usually dominated by the CVP. This CVP may form inside the jet and persist far downstream from the jet exit hole [18]. The formation is delayed as the velocity ratio is increased [36]. The reason for the formation is still under research and no general consensus exists about it. Different mechanisms have been proposed and a recent one is a two-dimensional model proposed by Muppidi and Mahesh [25] in Figure 2.3. In their model the initially circular jet has only out-of-plane velocity and the crossflow has only in-plane velocity. Their model explains how the crossflow moves the jet to its direction and as a consequence the leading and trailing edges are moved closer to each other. The latter induces the jet to expand in the radial direction to satisfy the mass conservation. The top and the bottom edges of the jet encounter strong shear and the result is the CVP. Their model also shows that the CVP does not need a pipe to develop. Moreover, the CVP is highly responsible for the jet cross section, especially in the far field [18]. The instantaneous behaviour of the CVP is asymmetric and unsteady [23].

The horseshoe vortices are similar in many ways to the vortices that are encoun-

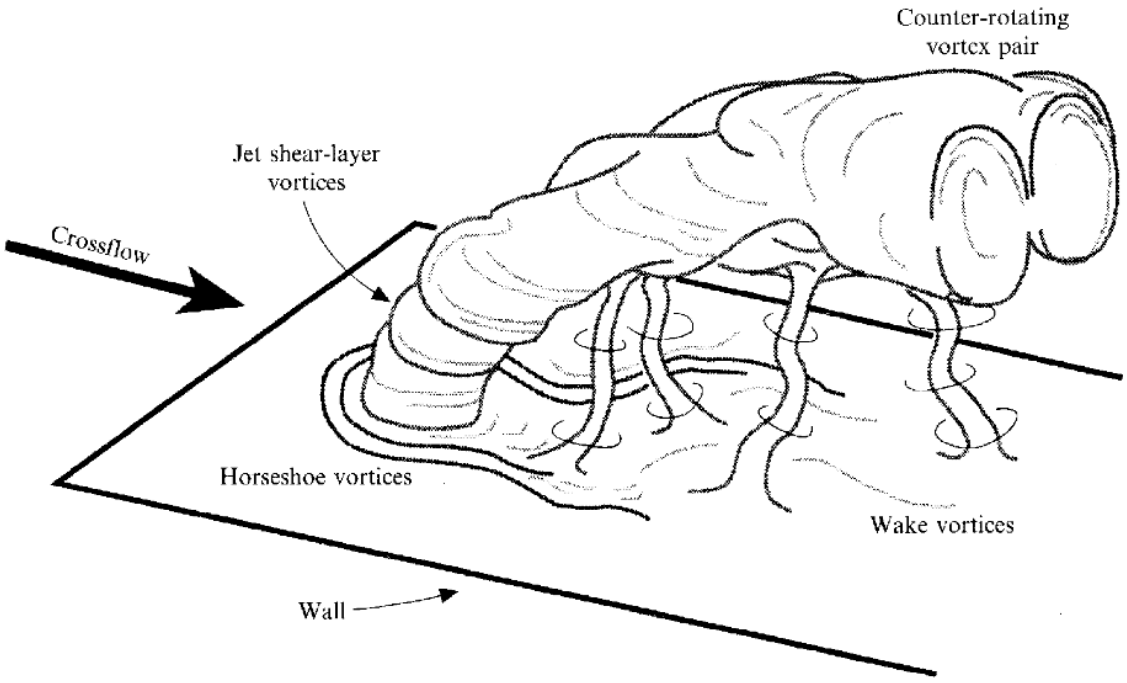

Figure 2.2 *A sketch of vortex structures in the jet in crossflow (Fric and Roshko [12]).*

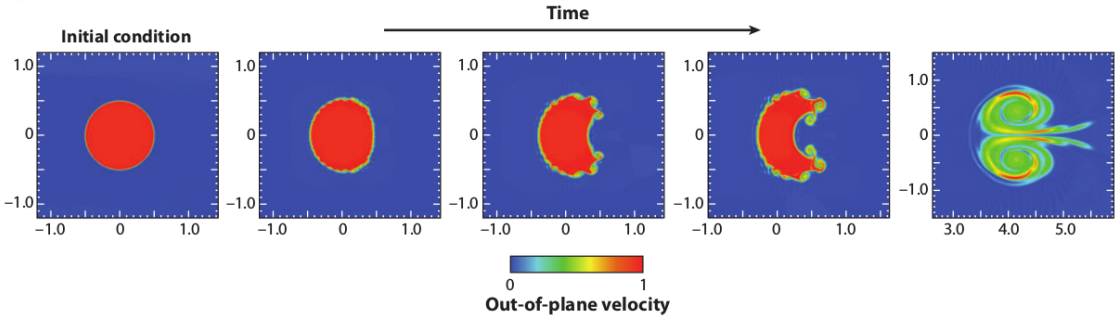

Figure 2.3 *Formation of counter-rotating vortex pair using a two dimensional model (Muppidi and Mahesh [25]).*

tered in a flow past a bluff body especially when the velocity ratio is high [15] while the wake vortices are fundamentally different. Fric and Roshko [12] explain that the horseshoe vortices result from the crossflow boundary layer approaching the jet leading edge. The boundary layer encounters an adverse pressure gradient which decelerates the flow and folds the boundary layer around the jet and form the horseshoe vortices. The wake vortices are observed downstream the jet exit hole between the jet leeward edge and the wall. Fric and Roshko have shown that the vorticity of the wake vortices originates from the crossflow boundary layer and they form periodically to either side of the jet in the spanwise direction. The wake vortices are consisted solely from the crossflow fluid [11].

When the velocity ratio is low, the interaction of the jet with the crossflow is domi-

nated by hairpin vortices. Mahesh [23] explains that the hairpin vortices form when the crossflow boundary layer vortices dominate the jet boundary layer vortices near the leading edge where they have opposite vorticity signs in the spanwise direction. Consequently, the jet boundary layer vortices are shed from the trailing edge and the hairpin vortices are formed.

2.3 Design variables

The number of design variables in the jet in crossflow configuration may be large and the optimal values may be chosen according to the desired properties of the application. Here, we present some of the most important design variables regarding film cooling. The purpose of film cooling is to cool down the wall and thus minimize the heat flux between the gas and the wall. The heat flux is given by

$$q = h\Delta T, \tag{2.4}$$

where h is the heat transfer coefficient and ΔT is the driving temperature potential. The heat transfer coefficient depends on the gas properties and the flow characteristics such as velocity and turbulence level. The jet injection causes disturbance to the flow and therefore it often increases the heat transfer coefficient in comparison to flow without injection. In film cooling the driving potential is generally assumed as the difference between adiabatic wall temperature and wall temperature ($\Delta T = T_{aw} - T_w$). One benchmark parameter for the efficiency is the film cooling efficiency which is given by

$$\eta = \frac{T_\infty - T_{aw}}{T_\infty - T_j}, \tag{2.5}$$

where T_∞ is the crossflow incoming temperature and T_j is the jet incoming temperature. The film cooling efficiency defines how well the gas temperature at the wall is cooled down. A unity value means that the gas temperature is at the jet incoming temperature and thus perfectly cooled while a zero value means that the gas at the wall is not cooled at all.

In film cooling applications the velocity ratio is low because the jet has to stay attached to the wall in order to provide the best thermal protection. In processes that require rapid mixing and high penetration, a high velocity ratio is desired. Thole et al. [37] showed that for a jet which is inclined 30 degrees the penetration and attachment scale with the momentum ratio

$$I = \rho_{jet} U_{jet}^2 / \rho_\infty U_\infty^2, \tag{2.6}$$

where ρ_{jet} is the jet density and ρ_∞ is the density of the crossflow. They identified three different regions for attachment: $I < 0.4$ where the jet remains attached, $0.4 < I < 0.8$ where the jet first detaches and then reattaches and $I > 0.8$ where the jet remains detached.

Common film cooling configuration contains both injection and compound angles because they spread the jet better and thus increase the cooling efficiency. Different injection angles were studied by Goldstein et al. [14] and later by Yuen and Martinez-Botas [45]. Yuen and Martinez-Botas investigated three injection angles, namely 30, 60 and 90 degrees with seven different blowing ratios from 0.33 to 2.0. They found out that the injection angle increases the spanwise averaged cooling efficiency and 30 degrees injection angle provides the best efficiency with all the blowing ratios they used in their experiments.

McGovern and Leylek [24] investigated different compound angles. Their study contained RANS simulations with four different compound angles of 0, 45, 60 and 90 degrees. They report how the structure of CVP differs between the compound angles. Without compound angle the CVP extracted from the mean field is symmetric. It becomes more and more asymmetric as the compound angle increases. At 90 degrees, the windward side vortex of the CVP vanishes completely, resulting in a single strong vortex. Jung and Lee [17] made experiments for compound angles of 0, 30, 60 and 90 degrees with velocity ratios 0.5, 1.0 and 2.0 for a row of jets. They report that the jets spread better and more uniform as the compound angle increases, especially with higher velocity ratios. Consequently, the compound angle yields to a higher, more efficient and more uniform cooling. However, McGovern and Leylek conclude that as the compound angle increases also the heat transfer coefficient is augmented. Therefore, the cooling efficiency alone is not sufficient to measure the overall efficiency of film cooling.

Efficient film cooling contains many other design variables which are not dealt in this work. For example, the shape of the hole has a major effect on the film cooling. Moreover, the spacings between the holes both in streamwise and spanwise directions are crucial design variables as well.

3. TURBULENCE MODELLING

In this section, the conservation equations which govern compressible flow are presented. Then the energy cascade which is a fundamental point of turbulence modelling is introduced and two different turbulence modelling approaches, namely RANS and LES are finally described.

3.1 Conservation equations

The thermodynamic behaviour is considered here as ideal gas. The ideal gas law is given by

$$p = \rho R T, \tag{3.1}$$

where p is the pressure, ρ is the density, R is the specific gas constant and T is the temperature.

The Navier-Stokes equations for compressible fluid with ideal gas properties can be written as:

$$\frac{\partial \rho}{\partial t} + \frac{\partial \rho u_j}{x_j} = 0 \tag{3.2}$$

$$\frac{\partial \rho u_i}{\partial t} + \frac{\partial \rho u_i u_j}{\partial x_j} + \frac{\partial p}{\partial x_i} = \frac{\partial \sigma_{ij}}{\partial x_j} \tag{3.3}$$

$$\frac{\partial \rho E}{\partial t} + \frac{\partial (\rho E + p) u_j}{\partial x_j} = \frac{\partial \sigma_{ij} u_i}{\partial x_j} - \frac{\partial q_j}{\partial x_j}, \tag{3.4}$$

where u is the velocity, σ_{ij} is the viscous stress, E is the total energy and q_j is the heat-flux. The fluid behaviour is assumed Newtonian and thus the viscous stress is linearly proportional to the strain rate. The viscous stress is then given by

$$\sigma_{ij} = 2\mu S_{ij} - \frac{2}{3}\mu \delta_{ij} S_{kk}, \tag{3.5}$$

where μ is dynamic viscosity, δ_{ij} is Kronecker delta and S_{ij} is the rate-of-strain tensor

$$S_{ij} = \frac{1}{2}\left(\frac{\partial u_i}{\partial x_j} + \frac{\partial u_j}{\partial x_i}\right). \tag{3.6}$$

The total energy and the heat-flux are given by

$$E = c_v T + \frac{1}{2} u_k u_k \tag{3.7}$$

$$q_j = -c_p \frac{\mu}{Pr} \frac{\partial T}{\partial x_j}, \tag{3.8}$$

where c_v and c_p are respectively the heat capacity in constant volume and constant pressure and Pr is the Prandtl number. The Prandtl number is defined as the ratio between kinematic viscosity and thermal diffusivity

$$Pr = \frac{\nu}{\alpha}. \tag{3.9}$$

In addition to the Navier-Stokes equations, we consider a transport equation for a passive scalar. The passive scalar may represent any physical quantity that does not affect the momentum equation. For example, temperature may be considered as a passive scalar when the temperature difference is small and the fluid properties can be considered as constant. The passive scalar equation can be written as

$$\frac{\partial \rho c}{\partial t} + \frac{\partial \rho u_j c}{\partial x_j} = \frac{\mu}{Sc} \frac{\partial^2 c}{\partial x_j^2}, \tag{3.10}$$

where c is the passive scalar and Sc is the Schmidt number. The Schmidt number expresses the ratio between kinematic viscosity and mass diffusivity

$$Sc = \frac{\nu}{\mathcal{D}}, \tag{3.11}$$

where $\mathcal{D}$ is the mass diffusivity.

3.2 Energy cascade

High Reynolds number flows contain a wide range of length scales which originate from turbulence. The largest scales are comparable with the characteristic length of the problem while the smallest scales are set by the viscous dissipation which is characterized by the Reynolds number. The higher Reynolds number yields to smaller length scales which leads to a wider range. Energy cascade theory gives an explanation to this phenomenon. The energy cascade was first proposed by Richardson's notion [31] in 1922 and it was later completed by Kolmogorov's hypotheses [19, 20] in 1941.

The idea of energy cascade is that the turbulence is composed of eddies of different

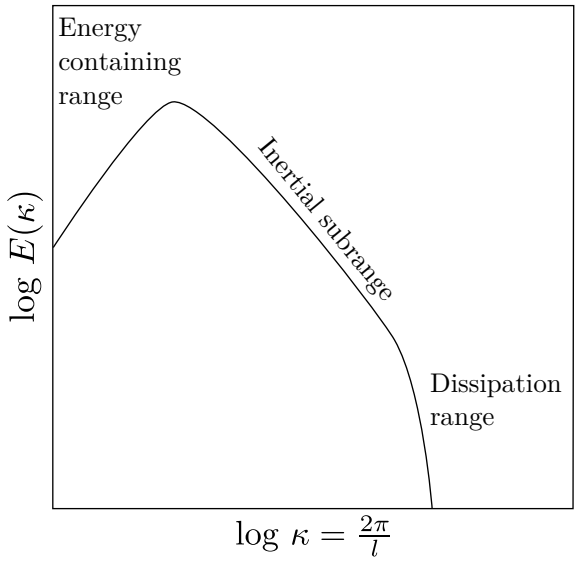

Figure 3.1 *Schematic of an energy spectrum in a high Reynolds number flow.*

sizes which are characterized by a length scale l and a velocity scale u. The characteristic length and velocity scale of the largest eddies are respectively of order of the characteristic length L and the characteristic velocity U of the problem. Consequently, in high Reynolds number flows the largest eddies have a high turbulence Reynolds number $Re = \dfrac{ul}{\nu}$ thus they are unstable and the effect of viscous forces are negligible. In the energy cascade, the kinetic energy enters the turbulence at the largest scales. Eventually, the largest eddies break up to smaller eddies and this process continues until the smallest length scale is reached where the viscous forces become significant and dissipate the kinetic energy to heat.

Figure 3.1 shows a schematic of energy spectrum and thus how the energy is distributed among the various length scales. The length scales are divided into three divisions which each have their own characteristics. First, the energy containing range is characterized by the large eddies which are highly dependent on the geometry and contain most of the energy. The small scale contains two ranges, namely inertial subrange and dissipation range. According to Kolmogorov's first hypothesis, they are statistically universal in the limit of high Reynolds number flows. This is a result of the chaotic length scale reducing process in which eddies lose memory of their initial geometry and direction. Kolmogorov's second hypothesis states that the eddies in inertial subrange are still large enough to remain unaffected by the viscous forces. Consequently, neither production nor dissipation occurs in the inertial subrange and therefore the energy is only transferred from large scales to small scales. As a result of independency both on geometry and viscosity the slope of such an inertial subrange can be characterized by a $-5/3$ slope. At the smallest scales, viscous forces are dominating and they dissipate the energy which is transferred

from larger scales to internal energy.

The energy cascade theory has some shortcomings and limitations. For example, the small length scales may remain anisotropic even in rather high Reynolds number flows and in contrast to the assumption, some part of the energy can be transferred also from the small scales to the large scales [28]. Nevertheless, the theory is a major finding in the field of turbulence studies.

3.3 Reynolds-averaged Navier-Stokes equations

The most common practice in industry is the Reynolds-averaged Navier-Stokes approach (RANS) which was proposed by Reynolds [30] in 1894. In RANS approach only the ensemble averaged equations are solved and the whole turbulence spectrum is modelled. Consequently, a much coarser computational mesh can be used. For RANS equations each instantaneous quantity is decomposed into average and fluctuation component

$$\phi = \overline{\phi} + \phi' \tag{3.12}$$

$$\overline{\phi} = \frac{1}{\Delta t}\int_t \phi(t)\, dT, \tag{3.13}$$

where $\overline{\phi}$ is the time average and ϕ' is the fluctuation component. The RANS equations are obtained by decomposing each quantity in conservation equations and applying following averaging rules

1. $\overline{\overline{\phi}} = \overline{\phi}$
2. $\overline{\phi + \varphi} = \overline{\phi} + \overline{\varphi}$
3. $\overline{\overline{\phi}\varphi} = \overline{\phi}\,\overline{\varphi}$
4. $\overline{\phi'} = 0$
5. $\overline{\phi\phi'} = \overline{\phi}\,\overline{\phi'} = 0.$

For the sake of simplicity only the incompressible equations are presented here:

$$\frac{\partial \overline{u}_i}{\partial x_i} = 0 \tag{3.14}$$

$$\frac{\partial \overline{u}_i}{\partial t} + \frac{\partial \overline{u}_i\,\overline{u}_j}{\partial x_j} + \frac{1}{\rho}\frac{\partial \overline{p}}{\partial x_i} = \frac{1}{\rho}\frac{\partial \overline{\sigma}_{ij}}{\partial x_j} - \frac{\partial \overline{u_i' u_j'}}{\partial x_j} \tag{3.15}$$

$$\frac{\partial \overline{c}}{\partial t} + \frac{\partial \overline{u}_i \overline{c}}{\partial x_i} = \frac{\nu}{\mathrm{Sc}} \frac{\partial \overline{c^2}}{\partial^2 x_i} - \frac{\partial \overline{u_i' c'}}{\partial x_i}. \tag{3.16}$$

The last terms in Equations (3.15) and (3.16) yield from the advection term because

$$\overline{\phi_i \phi_j} = \overline{(\overline{\phi}_i + \phi_i')(\overline{\phi}_j + \phi_j')} = \overline{\overline{\phi}_i \overline{\phi}_j} + \overline{\overline{\phi}_i \phi_j'} + \overline{\phi_i' \overline{\phi}_j} + \overline{\phi_i' \phi_j'} = \overline{\phi}_i \overline{\phi}_j + \overline{\phi_i' \phi_j'}. \tag{3.17}$$

The terms $\overline{u_i' u_j'}$ and $\overline{u_i' c'}$ are called Reynolds stress and turbulent scalar flux. They have to be modelled for the closure of the equation system.

Most RANS models use Boussinesq hypothesis to model the Reynolds stress which is given by

$$\overline{u_i' u_j'} = \frac{2}{3} k \delta_{ij} - \nu_t \left(\frac{\partial \overline{u}_i}{\partial x_j} + \frac{\partial \overline{u}_j}{\partial x_i} \right), \tag{3.18}$$

where $k = \frac{1}{2}\overline{u_i' u_i'}$ is the turbulence kinetic energy and ν_t is the turbulence eddy viscosity. The eddy viscosity models assume that the Reynolds stresses are proportional to the mean strain rate and the behaviour is isotropic. Many different models have been proposed to model the turbulence viscosity but usually their performance is limited to certain types of flows and no universal models exist.

The turbulent scalar flux $\overline{u_i' c'}$ is usually modelled by using standard gradient diffusion hypothesis (SGDH) which is given by

$$\overline{u_i' c'} = -\mathcal{D}_t \frac{\partial \overline{c}}{\partial x_i}, \tag{3.19}$$

where $\mathcal{D}_t$ is the turbulent diffusivity. The model assumes that the turbulent scalar flux is aligned with the mean scalar gradient and the behaviour is isotropic. The turbulent scalar flux and the SGDH are further discussed in Section 5.7 and 5.8.

3.4 Large eddy simulation

The large eddy simulation (LES) was first proposed by Smagorinsky [35] in 1963. In LES the flow is decomposed to directly resolved large scale motion and filtered small scale motion (Figure 3.2). This low-pass filtering is motivated by the Kolmogorov's hypotheses (see Section 3.2) which assume that in high Reynolds number flows the small scale eddies are statistically isotropic. Therefore, in LES the small scale filtering may yield to more universal models than the RANS approach. The computational expense of LES remains moderate in comparison with DNS because the small scales are modelled. Modelling small scales allows using a coarser computational mesh and higher time step.

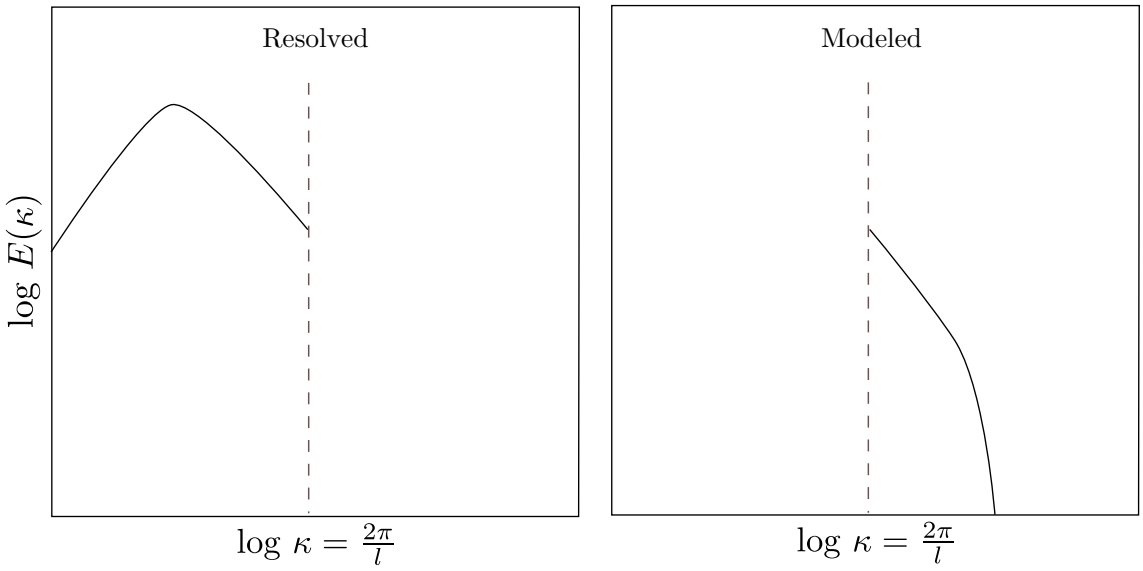

Figure 3.2 *Schematic of the energy spectrum in LES.*

Mathematically, LES decomposition is given by

$$\phi_i = \overline{\phi}_i + \phi_i', \tag{3.20}$$

where $\overline{\phi}_i$ is the large scale and ϕ_i' is the small scale. The resolved large scale motion is given by

$$\overline{\phi}(\mathbf{x}, t) = \int_{-\infty}^{\infty}\int_{-\infty}^{\infty} \phi(\boldsymbol{\xi}, t')G(\boldsymbol{x} - \boldsymbol{\xi}, t - t')\, d\boldsymbol{\xi}\, dt', \tag{3.21}$$

where G is a convolution kernel which is a characteristic of the filter. Three properties are required from the filtering application

1. Conservation of constant

$$\overline{a} = a \tag{3.22}$$

$$\int_{-\infty}^{\infty}\int_{-\infty}^{\infty} G(\boldsymbol{\xi}, t')\, d\boldsymbol{\xi}\, dt' = 1 \tag{3.23}$$

2. Linearity

$$\overline{\phi + \varphi} = \overline{\phi} + \overline{\varphi} \tag{3.24}$$

3. Commutation

$$\frac{\overline{\partial\phi}}{\partial s} = \frac{\partial\overline{\phi}}{\partial s}. \tag{3.25}$$

Usually the filter employed in LES is a box filter of which the width Δ is the cell size

$$G(x - \xi) = \begin{cases} \frac{1}{\Delta}, & \text{if } |x - \xi| \leq \frac{\Delta}{2} \\ 0, & \text{otherwise} \end{cases} \tag{3.26}$$

and the filtered scale is called a subgrid-scale (SGS). In addition to the length scale filtering, a density weighted filter proposed by Favre [10] is used for the compressible equations to ease the modelling of the terms with density

$$\widetilde{\phi} = \frac{\overline{\rho\phi}}{\overline{\rho}}. \tag{3.27}$$

The two filters are applied to the conservation equations and the equations become

$$\frac{\partial\overline{\rho}}{\partial t} + \frac{\partial\overline{\rho}\widetilde{u_j}}{x_j} = 0 \tag{3.28}$$

$$\frac{\partial\overline{\rho}\widetilde{u_i}}{\partial t} + \frac{\partial\overline{\rho}\widetilde{u_i u_j}}{\partial x_j} + \frac{\partial\overline{p}}{\partial x_i} = \frac{\partial\overline{\sigma}_{ij}}{\partial x_j} \tag{3.29}$$

$$\frac{\partial\overline{\rho}\widetilde{E}}{\partial t} + \frac{\partial(\overline{\rho}\widetilde{u_j E} + \overline{p}\widetilde{u_j})}{\partial x_j} = \frac{\partial\overline{\sigma_{ij}u_i}}{\partial x_j} - \frac{\partial\overline{q}_j}{\partial x_j} \tag{3.30}$$

$$\frac{\partial\overline{\rho}\widetilde{c}}{\partial t} + \frac{\partial\overline{\rho}\widetilde{u_j c}}{\partial x_j} = \frac{\mu}{Sc}\frac{\partial^2\overline{c}}{\partial x_j^2}, \tag{3.31}$$

where the terms $\widetilde{u_i u_j}$, $\widetilde{u_j E}$ and $\overline{\sigma_{ij}u_i}$, $\widetilde{u_j c}$ have to be modelled to close the system of equations. In this work only models for the terms from the momentum and the passive scalar equations are further discussed because they are the only ones that appear in incompressible equations.

For SGS models the momentum equations and the passive scalar equation are usually given in the form

$$\frac{\partial\overline{\rho}\tilde{u}_i}{\partial t} + \frac{\partial\overline{\rho}\tilde{u}_i\tilde{u}_j}{\partial x_j} + \frac{\partial\overline{p}}{\partial x_i} = \frac{\partial\overline{\sigma}_{ij}}{\partial x_j} + \frac{\partial\rho\tau_{ij}}{\partial x_j}, \tag{3.32}$$

$$\frac{\partial\overline{\rho}\tilde{c}}{\partial t} + \frac{\partial\overline{\rho}\tilde{u}_j\tilde{c}}{\partial x_j} = \frac{\mu}{Sc}\frac{\partial^2\overline{c}}{\partial x_j^2} + \frac{\partial\rho q_j}{\partial x_j} \tag{3.33}$$

where τ_{ij} is the filtered momentum field and q_j is the filtered passive scalar flux

$$\tau_{ij} = \widetilde{u_i u_j} - \tilde{u}_i\tilde{u}_j \tag{3.34}$$

$$q_j = \widetilde{u_i c} - \tilde{u}_i\tilde{c}. \tag{3.35}$$

In most common SGS models the Boussinesq hypothesis is used in an analogous manner to the RANS modelling. The filtered momentum is then given by

$$\tau_{ij} - \frac{1}{3}\tau_{kk}\delta_{ij} = -2\nu_{SGS}\overline{S}_{ij}, \tag{3.36}$$

where ν_{SGS} is the SGS viscosity. The first SGS model proposed by Smagorinsky [35]

is given by

$$\nu_{SGS} = (C_s\Delta)^2|\overline{S}|, \tag{3.37}$$

where C_s is a constant and Δ is the cell size which is usually the cube root of the cell's volume. Smagorinsky model remains one of the most used SGS models due to its simplicity. However, the model has its drawbacks such as erroneous near wall behaviour, flow dependent constant C_s and it is not suitable for transitional flows [13]. More advanced Smagorinsky models have been proposed to overcome the drawbacks with a damping function near the wall and by using a dynamical variable instead of a constant.

An alternative eddy viscosity model has been recently proposed by Vreman [40]. Vreman shows that the model performs better in transitional and mixing layer flows at high Reynolds number than the Smagorinsky model. Moreover, the near wall behaviour is appropriate. He modelled the eddy viscosity as

$$\nu_{SGS} = 2.5C_s^2\sqrt{\frac{B_\beta}{\alpha_{ij}\alpha_{ij}}}, \tag{3.38}$$

with

$$\alpha_{ij} = \frac{\partial u_j}{\partial x_i}, \tag{3.39}$$

$$\beta_{ij} = \Delta_m^2\alpha_{mi}\alpha_{mj}, \tag{3.40}$$

$$B_\beta = \beta_{11}\beta_{22} - \beta_{12}^2 + \beta_{11}\beta_{33} - \beta_{13}^2 + \beta_{22}\beta_{33} - \beta_{23}^2. \tag{3.41}$$

For the filtered scalar flux the simplest model is given by

$$q_j = -\frac{\nu_{SGS}}{Sc_{SGS}}\frac{\partial\tilde{c}}{\partial x_j}, \tag{3.42}$$

where Sc_{SGS} is the SGS Schmidt number which is a constant $Sc_{SGS} \approx 1$.

4. ASYMMETRIC JET IN CROSSFLOW

In this chapter, the present jet in crossflow configuration is described. The configuration is studied both by carrying out an experiment and a numerical simulation. Both approaches are presented here.

4.1 Problem details

The present jet in crossflow configuration includes the most relevant physics of a film cooling application. The velocity and the momentum ratio are both set to unity. The crossflow forms a turbulent boundary layer before interacting with the jet and the boundary layer thickness is $\delta_{99} \approx D$. Figure 4.1 shows the geometry which has an injection angle of 30 degrees and a compound angle of 30 degrees. The dimensions are normalized with the jet hole diameter D. The hole axial length is $l = 4.1D$. The jet feeding plenum is included into the geometry, both in the experimental set up and in the computational domain. The distances between the jet and the duct corners are chosen to minimize their impact on the interaction of the jet with the crossflow ($l_{z+} = 5.2D, l_{z-} = 12.1D$).

4.2 Experimental approach

Experiments have been performed by Ryan et al. [34] using Magnetic Resonance Imaging (MRI) techniques which provide three dimensional fields of the mean velocity and the mean contaminant concentration. Contaminated (copper sulphate) water is fed from one inlet and pure water from the other inlet. The mixing of the contaminant is analogous to the heat transfer and therefore relevant to the film cooling applications in which temperature is of great interest. The Schmidt number is $Sc = 1500$ between water and copper sulphate. A boundary layer trip is used to create the crossflow turbulent boundary layer and the jet Reynolds number is $Re_j = 2900$. The spatial resolution of the rectangular voxels used in MRI experiments are $\Delta x \approx 0.1D$ in all directions.

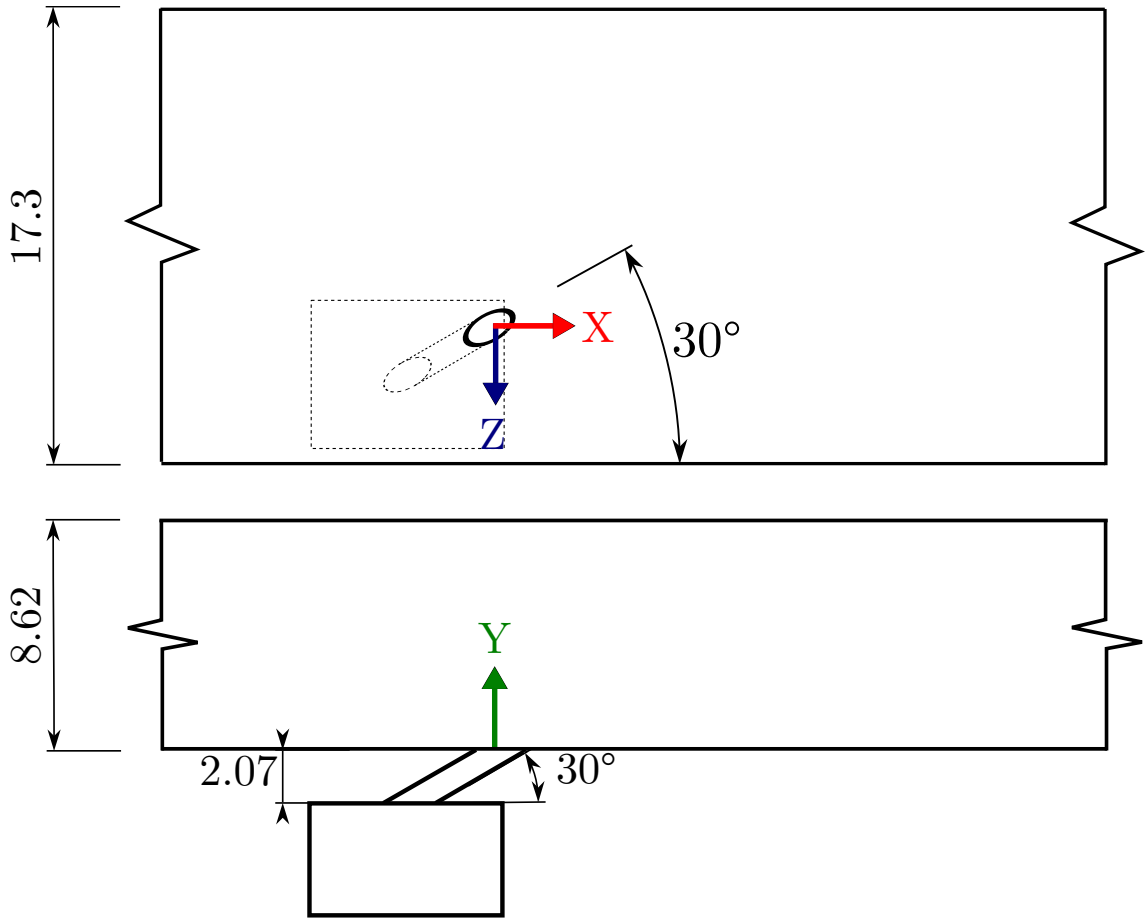

Figure 4.1 *Geometry of the present jet in crossflow configuration and coordinate system. The lengths are non-dimensionalized with the jet hole diameter D.*

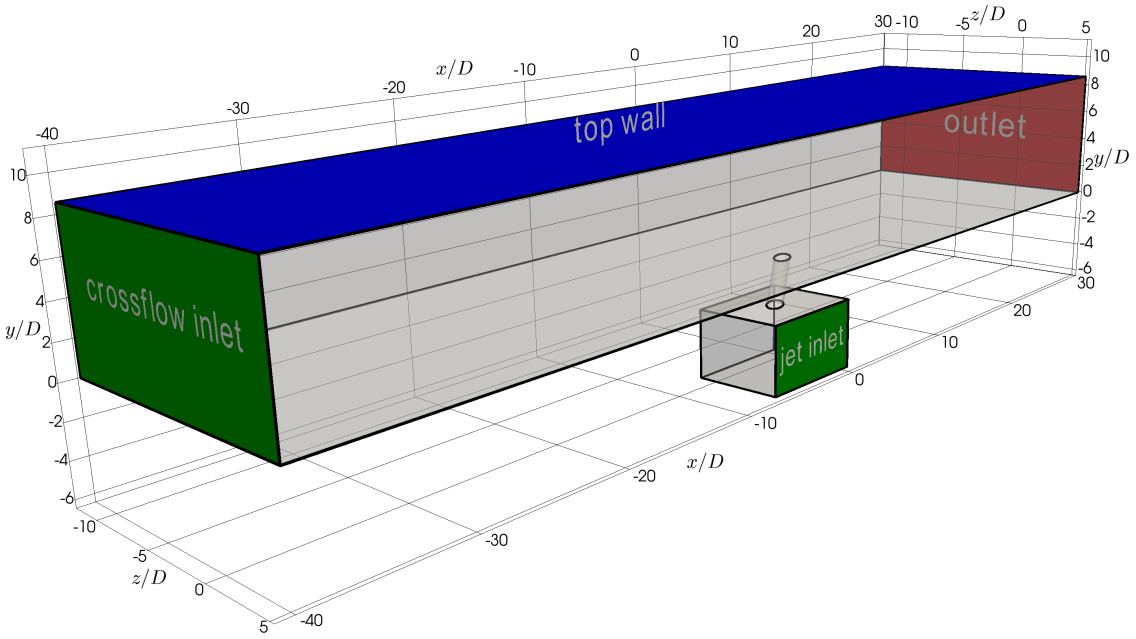

Figure 4.2 *Computational domain and boundary conditions.*

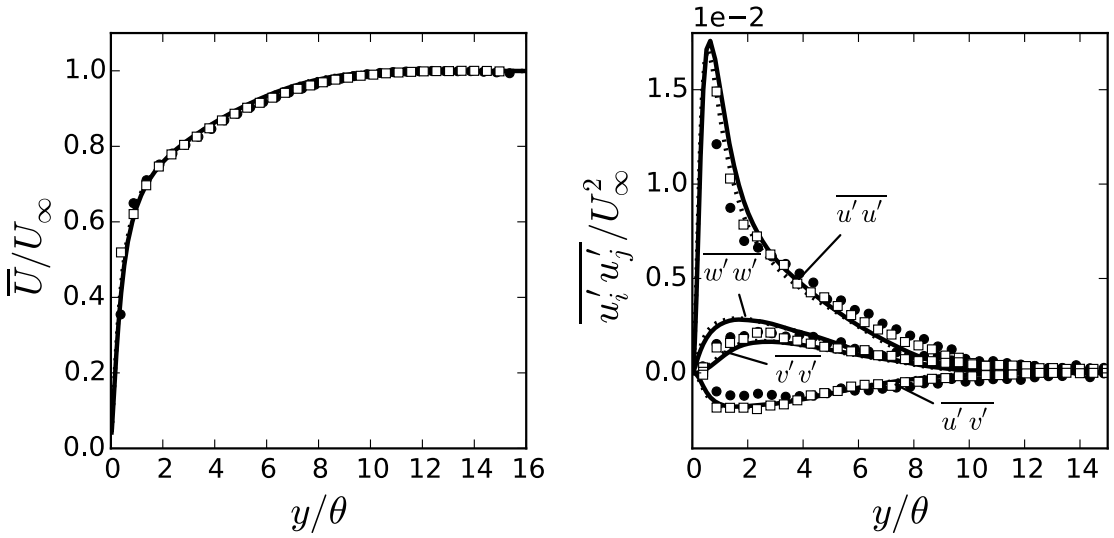

Figure 4.3 *Comparison of boundary layer with the present LES (lines) and PIV experiment (markers) by Coletti et al. [8] at two streamwise locations upstream the interaction. Solid line, square $x = -13.7D$ and dot line, circle $x = -7.2D$.*

4.3 Numerical approach

The numerical domain and boundary conditions used in the present simulation are given in Figure 4.2. The crossflow inlet is $40D$ upstream the jet exit hole and the outlet is $30D$ downstream the hole. At the walls (grey), no-slip condition is enforced for the velocity and a zero flux condition is imposed on the scalars. At the top wall a slip boundary condition is used. Thus, all quantities have a null gradient. This relieves the computational expense because the boundary layer is not resolved. At the outlet, a uniform pressure is imposed. The inlet for the jet is given on one side of the jet feeding plenum. A uniform boundary condition is used for all quantities besides pressure which is a result of the simulation.

The inflow boundary condition in unsteady turbulent simulations such as the crossflow inlet is challenging because in addition to the mean quantities, the time dependent fluctuation has to be provided at each time step. In the present simulation, a synthetic turbulence is used to generate a turbulent boundary layer. The generator uses a method proposed by Xie and Castro [43] with the modifications by Touber and Sandham [38]. The turbulent boundary layer has exactly the same characteristics as in the simulation by Bodart et al. [4] and therefore the generator uses the same parameters as in their simulation. A length of $40D$ is required upstream the jet interaction to recover a fully physical behaviour. The jet Reynolds number $Re_j = 5800$ is doubled in comparison to the experiments to trigger and sustain a fully turbulent boundary layer. The resulting boundary layer is compared at two locations upstream from the jet exit hole with the particle image velocimetry (PIV)

experiments by Coletti et al. [8] in which the same channel geometry and boundary layer thickness were used. The results are shown in Figure 4.3 and the agreement is excellent between the simulation and the experiment. The wall normal distance is normalized with the momentum thickness which is given by

$$\theta = \int_0^\infty \frac{\overline{U}}{U_\infty}\left(1 - \frac{\overline{U}}{U_\infty}\right) dy. \tag{4.1}$$

The simulation is initialized by running three additional simulations. First a RANS simulation is used to determine the required first cell size at the wall. Then two LES are carried out to generate the initial condition of the final mesh. LES mesh sizes are respectively 1 % and 10 % from the final mesh size.

The Charles^X solver is used in the present simulation. It is a compressible LES solver for unstructured meshes and with a finite volume approach to discretize the equations. The solver was initially developed at the Center for Turbulence Research and it has been shown to scale well on massively parallel architectures (see Appendix A). Although an incompressible solver is the natural tool to represent an experiment with water, we perform a low Mach number simulation with a perfect gas. This is also motivated by upcoming simulations in the future which may include compressibility effects encountered in the aeronautical applications. In these simulations, we use Vreman model for SGS viscosity and the simple gradient diffusion hypothesis (Equation 3.19) for the filtered scalar flux with $Sc_{SGS} = 0.9$. *A posteriori* results show that the SGS contribution is negligible in the present simulation.

For the spatial integration Charles^X uses a blend of two schemes depending on the quality of the mesh to ensure the accuracy and stability of the simulation. A blending factor which weights between the schemes is calculated once at the beginning of the simulation. At the regions of high quality mesh a non-dissipative central scheme is preferred and at the low quality regions upwind scheme is preferred. The central scheme is fourth order and upwind scheme is second order. Charles^X uses explicit third order Runge Kutta algorithm for the time integration. For the explicit time integration schemes it is important to meet the Courant-Friedrichs-Levy (CFL) condition which limits the time step. The CFL condition states that a wave may travel only one cell size during one time step or otherwise the results are incorrect. The CFL condition used in the present simulation is given by

$$\frac{(c+u)\Delta t}{\Delta x} < 1.6, \tag{4.2}$$

where c is the speed of sound, Δt is the time step and Δx is the cell size.

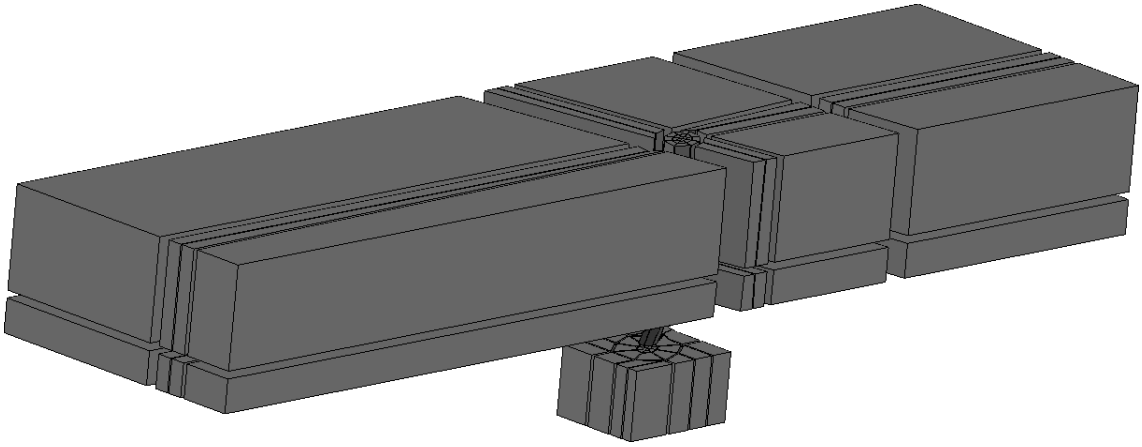

Figure 4.4 *Blocking structure of the mesh.*

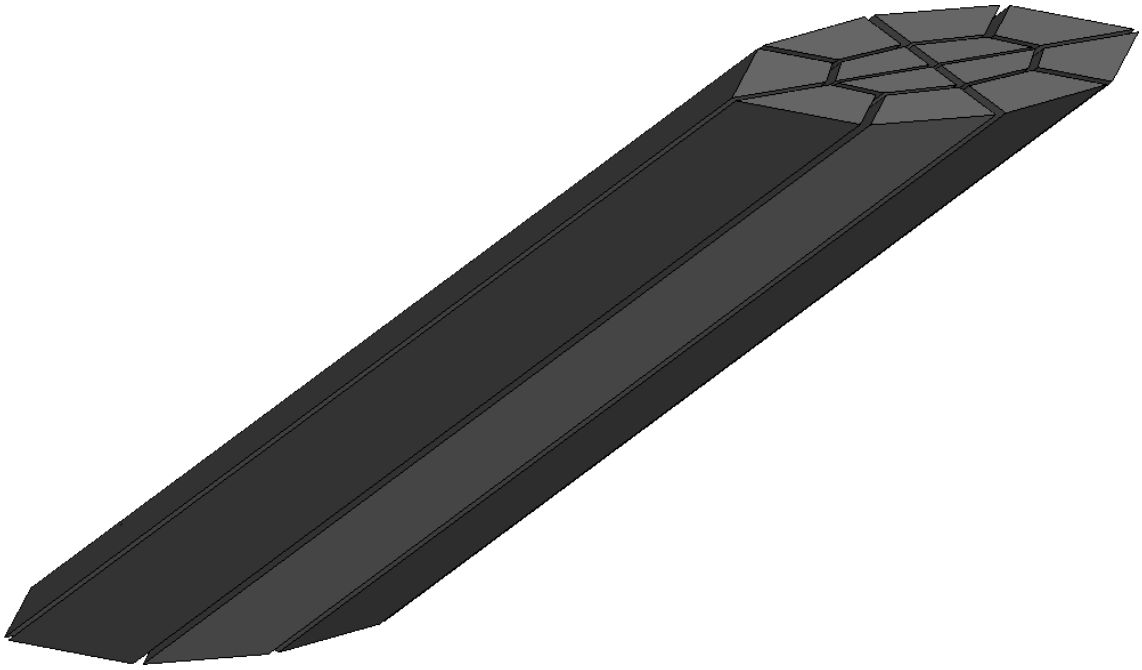

Figure 4.5 *Blocking inside the cooling hole.*

In addition to the Navier-Stokes equations a transport equation for a passive scalar is solved. The passive scalar is used to study the mixing of the jet and the crossflow which is analogous to the heat transfer. The Schmidt number is set to unity which is significantly different than in the experiments (1500). This is motivated by two reasons. Firstly, we want to keep the smallest scales of momentum and diffusion in the same order because we do not want to rely too much on the simple SGS model for the filtered scalar flux. Secondly, the unity Schmidt number represents a realistic Prandtl number for many gases such as air. The passive scalar concentration is set to unity at the jet inlet and zero at the crossflow inlet.

The computational mesh contains overall 101 million cells which are all hexahedral

Table 4.1 *Characteristic cell sizes and dimensionless first cell size in wall units thus normalized with U_τ/ν. x is streamwise direction, y is wall normal direction and z is spanwise direction.*

				Average			Maximum		
region	$\Delta x/D$	$\Delta y/D$	$\Delta z/D$	Δx^+	Δy^+	Δz^+	Δx^+	Δy^+	Δz^+
Inflow	0.081	0.016	0.016	7.9	0.4	1.6	32.0	1.5	6.4
Jet Hole	0.001	0.016	0.009	2.1	0.4	2.2	6.1	1.0	6.3
Interaction	0.016	0.016	0.016	3.2	0.8	3.2	6.3	1.5	6.4

type. The cells are divided as follows: the channel has 82 million cells, the cooling hole has 17 million cells and the plenum has 2 million cells. The mesh is initially a structured mesh which contains 42 blocks and it is later converted to unstructured format for the solver. The blocking is shown in Figure 4.4 and the O-grid blocking which is used inside the pipe is shown in Figure 4.5. The walls are resolved thus the first wall normal cell size is close to unity $y^+ \approx 1$. The wall distance is given by

$$y^+ = \frac{yU_\tau}{\nu}, \tag{4.3}$$

where U_τ is the friction velocity $U_\tau = \sqrt{\tau_w/\rho}$ and τ_w is the wall shear stress. The mesh is finest at the following regions: crossflow inflow at the bottom of the channel, inside the jet hole and at the region of jet and crossflow interaction. Outside these regions the mesh cell size is smoothly growing. The non-dimensional wall units and characteristic cell sizes inside the described regions are shown in Table 4.1.

5. RESULTS

This chapter shows the results of the present large eddy simulation. Firstly, the instantaneous flow field quantities are presented. Secondly, the simulation is validated with the experiment and the mean flow field is investigated. Finally, the evolution of the turbulent scalar flux is studied. In particular we investigate the turbulent scalar flux transport equation.

5.1 Instantaneous field

The instantaneous shape of the jet can be observed by looking at the passive scalar concentration contours. Figure 5.1 shows the instantaneous contours on planes normal to spanwise direction at $z = -0.5D$. The three planes correspond to three different time frames. The passive scalar concentration is zero (black) at the crossflow inlet and unity (white) at the jet inlet. The crossflow is coming from the left and interacts with the jet that is ejecting from a hole that is both inclined and skewed 30 degrees. The crossflow bends the jet shortly after the injection to its direction which creates strong shear at the interface between the jet and the crossflow. Consequently, the jet shear layer vortices are formed on the windward side of the jet.

The jet cross section is observed on planes normal to streamwise direction in Figure 5.2. The three columns correspond to the same time frames as in previous Figure 5.1 and the rows are four different locations downstream the jet exit hole: $x = 1D$, $3D$, $5D$ and $7D$. The first row (a) shows the forming stronger vortex of the CVP. In the next planes (b) the shape is dominated by two circular regions which correspond to the CVP. Further downstream in planes (d) the shape has evolved into a single circular region of which the center seems to halt on approximately at $z = -0.5D$.

Usually, the vortices are observed in the regions of high vorticity

$$\omega_i = \frac{1}{2}\left(\frac{\partial u_i}{\partial x_j} - \frac{\partial u_j}{\partial x_i}\right). \tag{5.1}$$

Unfortunately, high vorticity may also be encountered in flows in which vortices

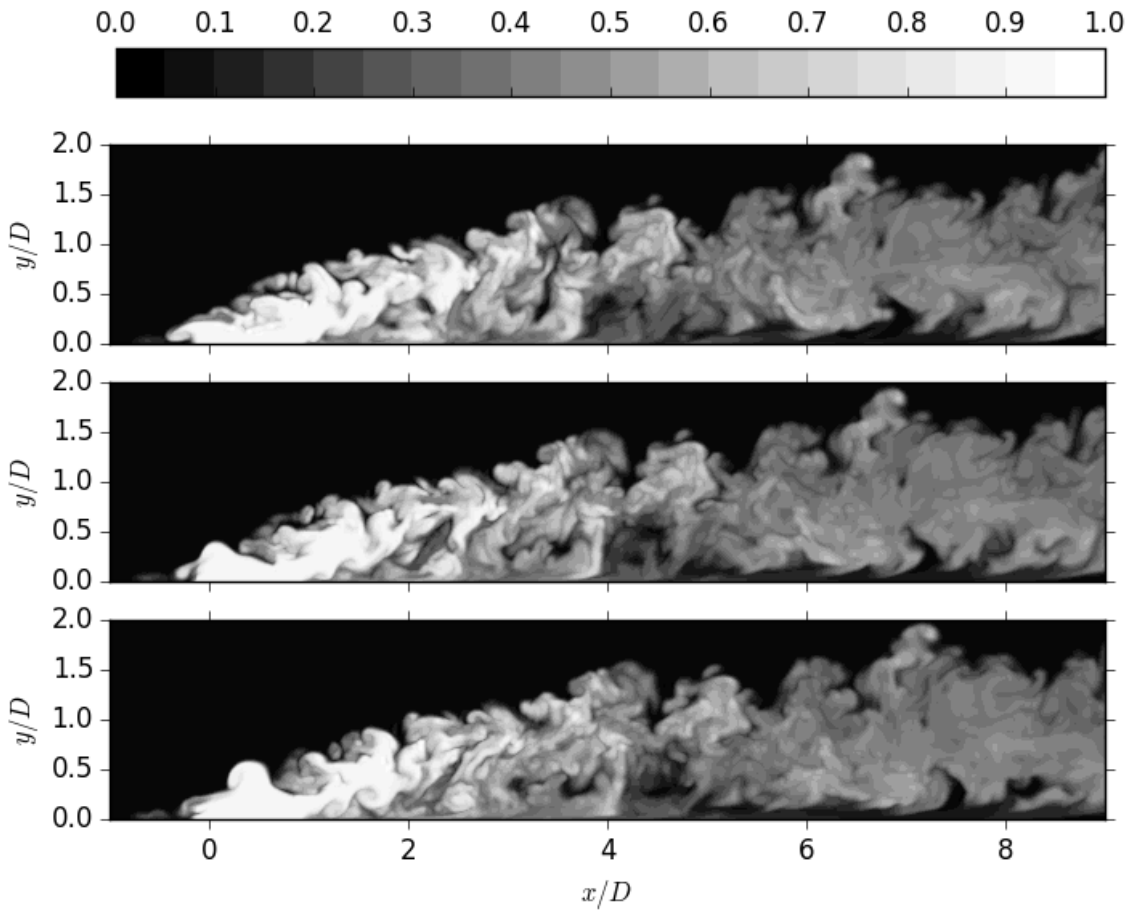

Figure 5.1 *Instantaneous contours of passive scalar concentration on plane normal to spanwise direction at $z = -0.5D$. Three different time frames.*

are not present at all. Therefore, more advanced methods are required to identify coherent vortical structures. Consequently, Hunt et al. [16] proposed Q-criterion which defines the vortex as a region where the magnitude of the vorticity dominates the magnitude of the rate-of-strain thus

$$Q = \frac{1}{2}(\omega_i\omega_i - S_iS_i). \tag{5.2}$$

Figure 5.3 shows two isocontours of Q-criterion from the instantaneous field. Plane (a) is normal to spanwise direction and plane (b) is normal to wall direction. The contours are coloured with the passive scalar concentration which is red at the channel inlet and blue at the jet inlet. The isocontour value in plane (a) is smaller than in plane (b) and therefore more structures are visible.

The developing turbulent crossflow boundary layer is approaching at the bottom of the channel and right before the leading edge it encounters an adverse pressure gradient from the jet which decelerates the flow and wraps the boundary layer

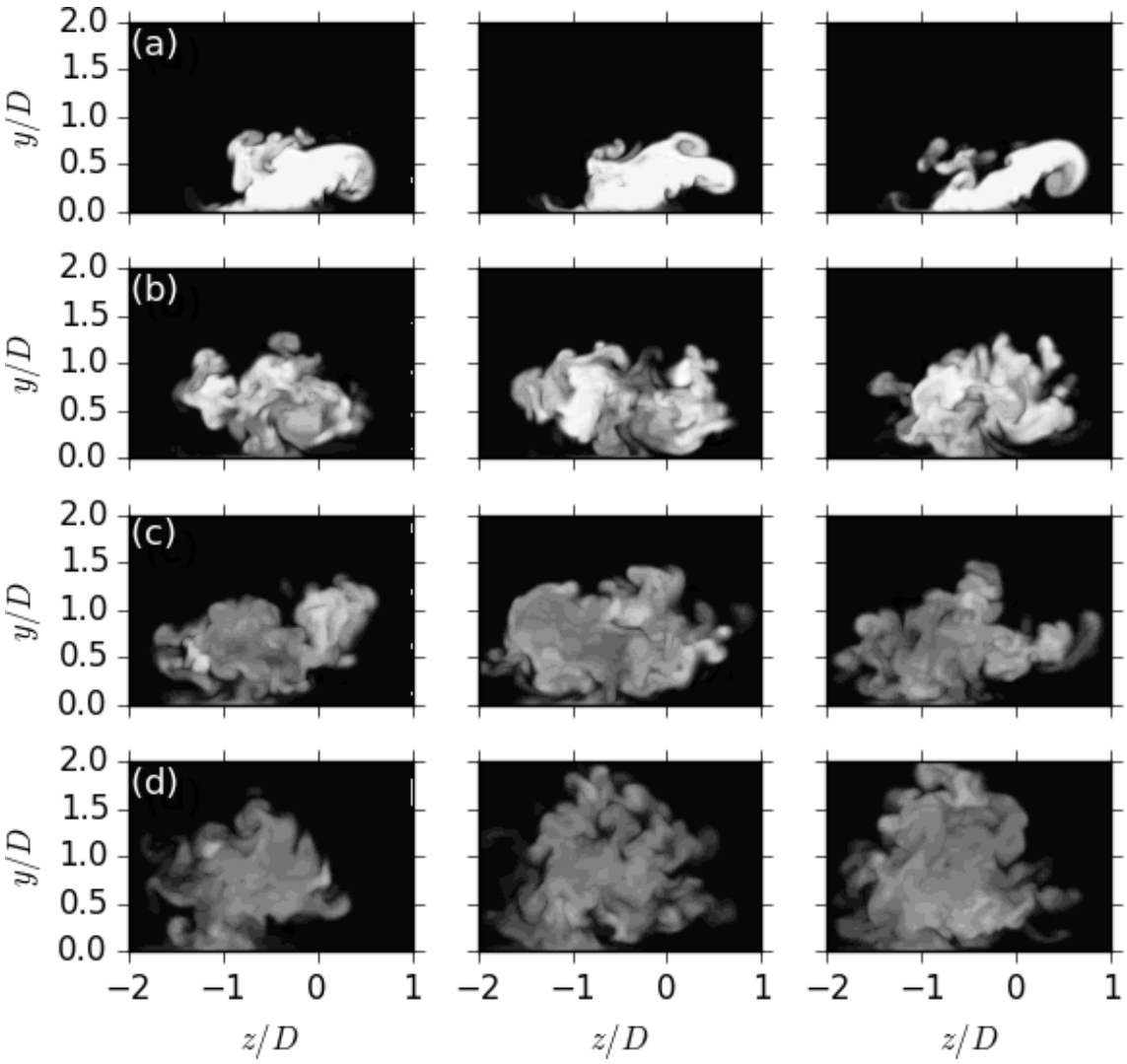

Figure 5.2 *Instantaneous contours of passive scalar on plane normal to streamwise direction at (a) $x = 1D$, (b) $x = 3D$, (c) $x = 5D$, (d) $x = 7D$. Same time instants as in Figure 5.1.*

around it and forms the horseshoe vortices. A single asymmetric horseshoe vortex is observed in plane (b) with a longer leg on the negative z side than on the positive z side. The flow has to circumvent farther at the negative z side because the compound angle injection creates a larger pressure gradient region there.

At the interface between the plenum and the hole an elliptical shaped ring vortex is observed. Ziefle and Kleiser [46] explain that the sharp angle between the interface of the plenum and the hole leads to separation and recirculation inside the hole which is responsible for the ring vortex. The separation region grows constantly bigger when going downstream inside the hole. After the jet exit hole, the jet shear layer vortices are formed and they grow radially in size and enhance the mixing of the jet and crossflow. The shear layer vortices seem to break up approximately after

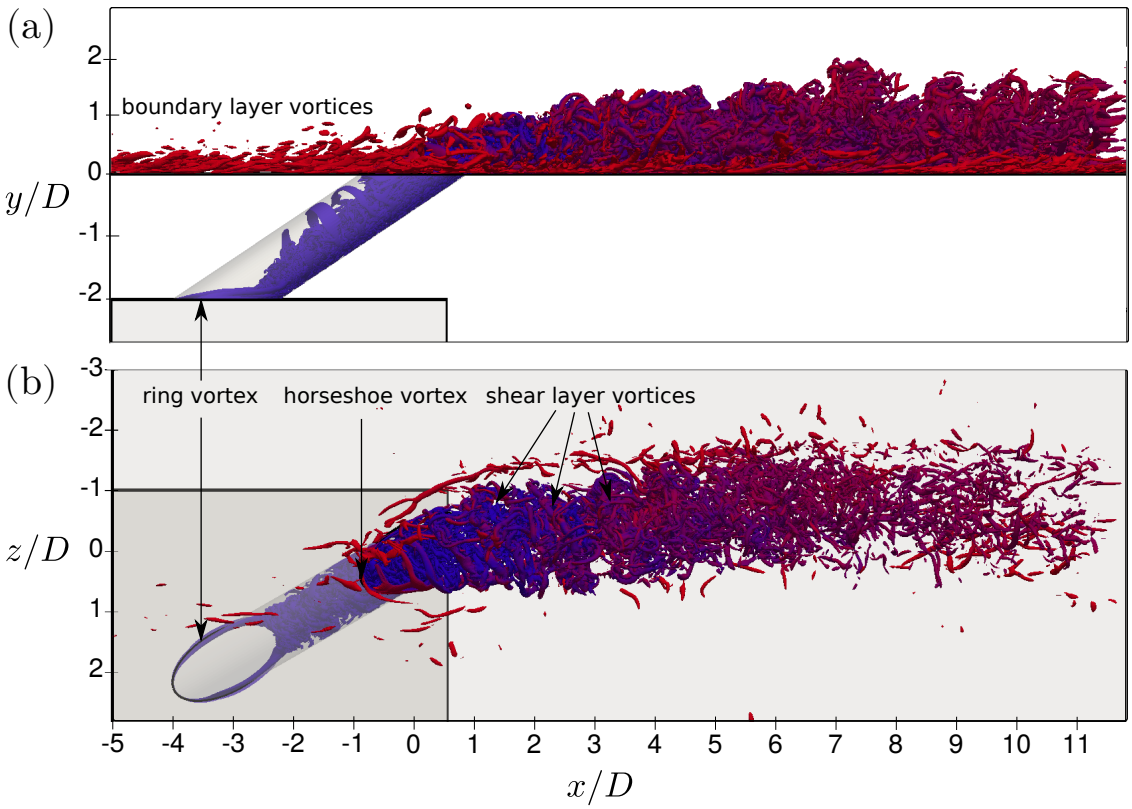

Figure 5.3 *Instantaneous isocontour of Q-criterion coloured with passive scalar concentration. (a) side view $Q = 1.2\,U_{jet}^2/D^2$, (b) top view $Q = 4.7\,U_{jet}^2/D^2$.*

$x = 5D$ and thereafter the structure of the flow is more isotropic.

5.2 Statistical sampling and convergence

A statistical analysis is carried out in the present simulation, once it has reached a statistically steady state. Statistical sampling is performed to gather the time averaged mean flow field. The samples are collected at the regular intervals of every 20 time steps. The simulation is carried out for 252 time units $T = D/U_{jet}$ and altogether 85 000 samples are collected.

The statistical convergence can be estimated by monitoring the target quantities during the simulation. Figure 5.4 shows residuals of the mean velocity magnitude and turbulence kinetic energy on a streamwise profile. The residual is given by

$$\mathrm{res}_\phi = 1 - \frac{\phi}{\phi_N}, \tag{5.3}$$

where ϕ is the target quantity and ϕ_N its value at the end of the simulation. The various colours show different accumulated time which goes from blue (beginning of

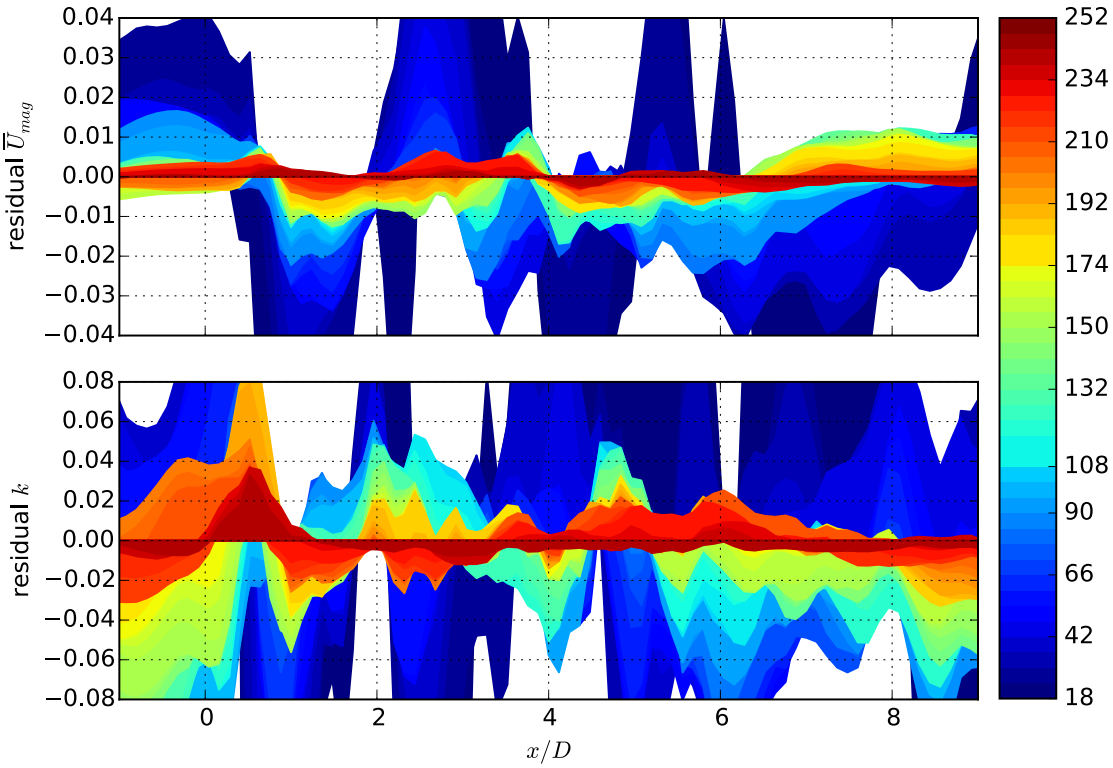

Figure 5.4 *Evolution of statistical convergence for velocity and turbulence kinetic energy in streamwise direction. Spanwise and wall normal components are held constant at* $y = 0.6D$, $z = -0.6D$.

the simulation) to red (end of the simulation). Both quantities are clearly approaching a steady state because the fluctuation is dampening as the simulation goes on. At the end of the simulation the velocity profile (first order moment) diverges less than 1 % and the turbulence kinetic energy profile (second order moment) diverges less than 4 % which gives an estimate of the uncertainty bounds of the averaging process.

5.3 Comparison to experiment

The mean flow field of the present simulation is compared against the experiments by Ryan et al. [34]. The mean velocity is compared inside the jet hole and at the region of the jet interaction with the crossflow. Moreover, the mean passive scalar concentration is compared with the mean contaminant concentration on the region of the interaction.

Figure 5.5 shows the mean axial velocity contours at six cut planes normal to the jet hole axis $\mathbf{n} = \begin{bmatrix} 0.75 & 0.5 & -0.433 \end{bmatrix}^T$. The cut plane locations are given in Figure 5.6.

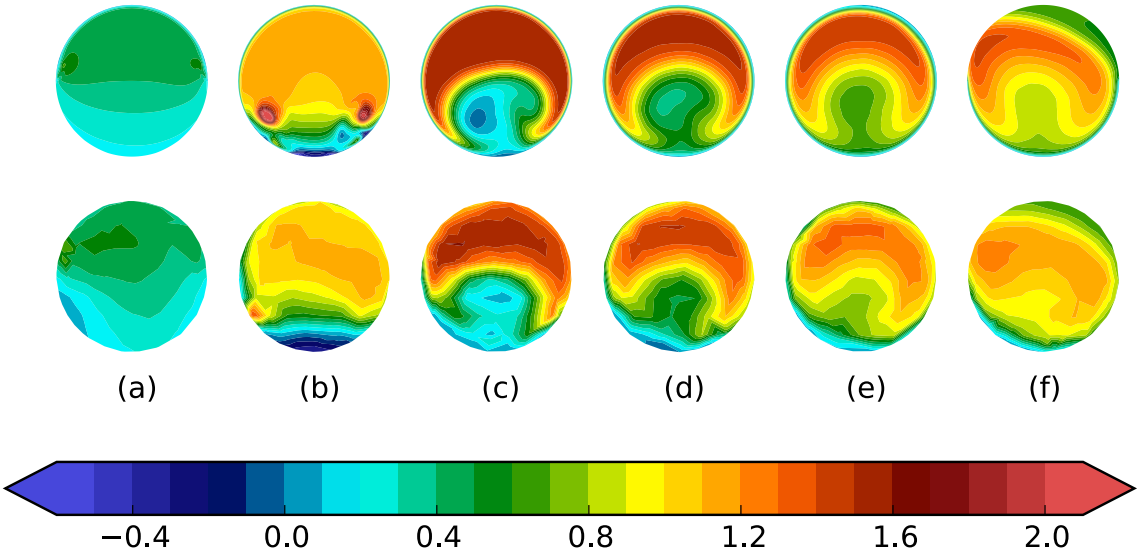

Figure 5.5 *Contours of the mean axial velocity U_n/U_{jet} on planes normal to the jet hole axis. Above is the simulation and below is the experiment. The plane locations are given in Figure 5.6.*

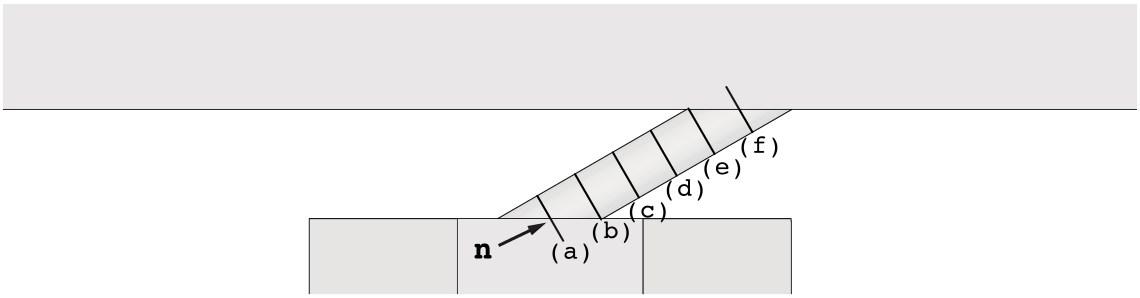

Figure 5.6 *Cut plane locations inside the hole and the direction of the normal to the hole axis.*

The planes above are extracted from the simulation and the planes below are taken from the experiment. The first plane (a) from the left is at the interface between the jet feeding plenum and the hole and the last plane (f) is at the interface of the hole and the channel. Note that the grid resolution in the experiment is coarse, only around eight voxels per cut plane.

In the first plane (a) the velocity is overall relatively low but already going downstream at the top of the cross section. The second plane (b) shows two small velocity peaks over two times the bulk velocity. This leads to the creation of a small counter-rotating vortex pair, which seems independent of the one formed in the interaction region. At the bottom of the section there is a strong backflow to the plenum where the maximum velocity is 0.8 times the bulk velocity. In the next plane (c) the flow has separated into two regions. At the top of the section the fluid is moving fast ($U/U_{jet} = 1.7$) upstream and at the bottom of the section the fluid is almost

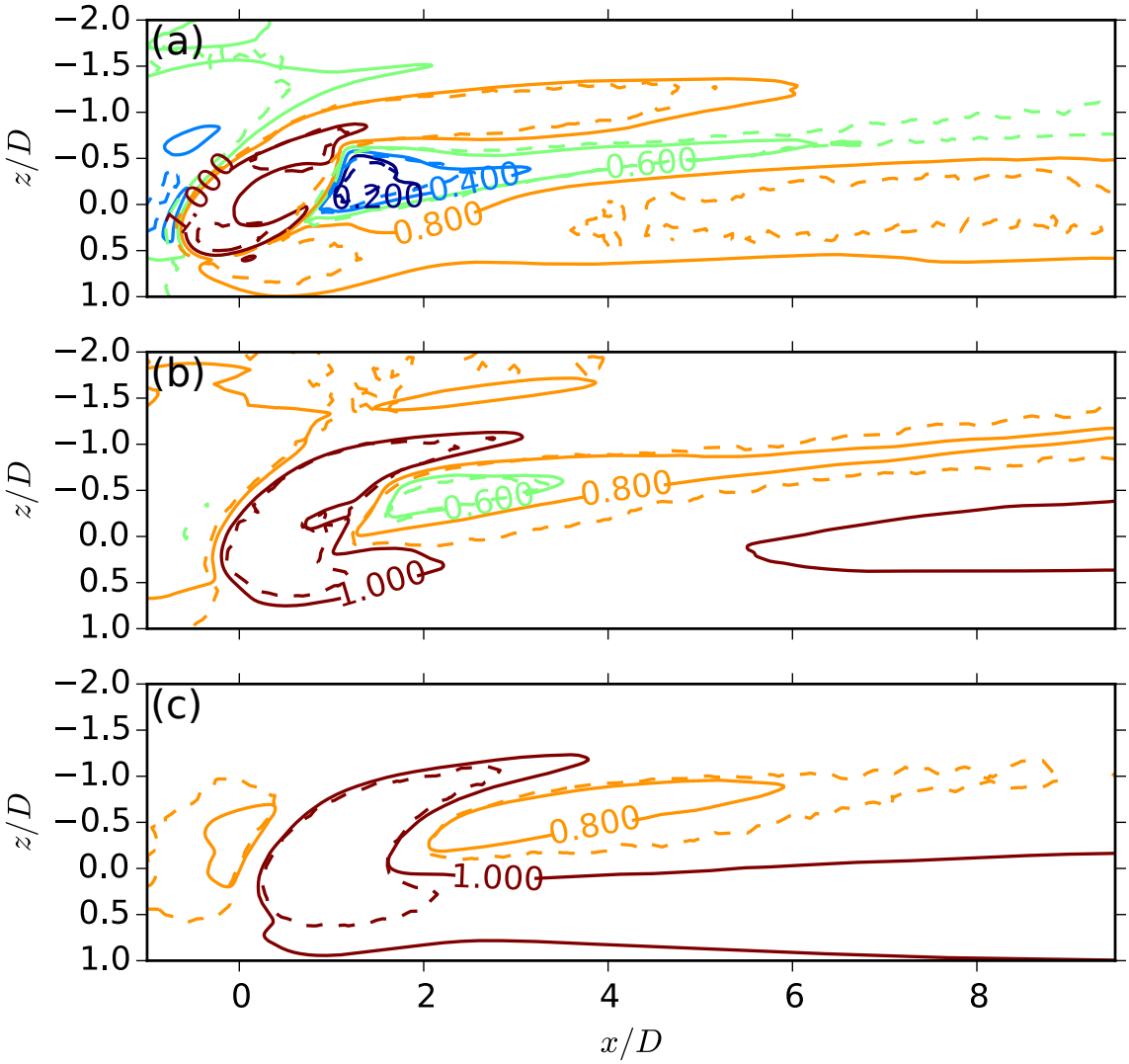

Figure 5.7 *Contours of the mean streamwise velocity U/U_{jet}. Planes are normal to wall direction at positions (a) $y = 0.1D$, (b) $y = 0.3D$ and (c) $y = 0.5D$. Solid line is the simulation and dashed line is the experiment.*

stagnated. In the next planes (d)-(f) the flow field is developing to more uniform. The planes look almost symmetric except the last one which is partially inside the channel.

The agreement between the experiment and the present simulation is good in general which demonstrates that the simulation is capable of capturing all the complex flow dynamics inside the hole before the interaction with the crossflow. In the experiments, the grid resolution is coarse and therefore the smallest details such as the small counter rotating vortex pair cannot be captured.

Figure 5.7 shows the mean streamwise velocity at the region of the interaction. The planes are normal to the wall direction at three locations: $y = 0.1D$, $0.3D$ and $0.5D$. The solid line is from the simulation and the dashed line is from the experiment. In

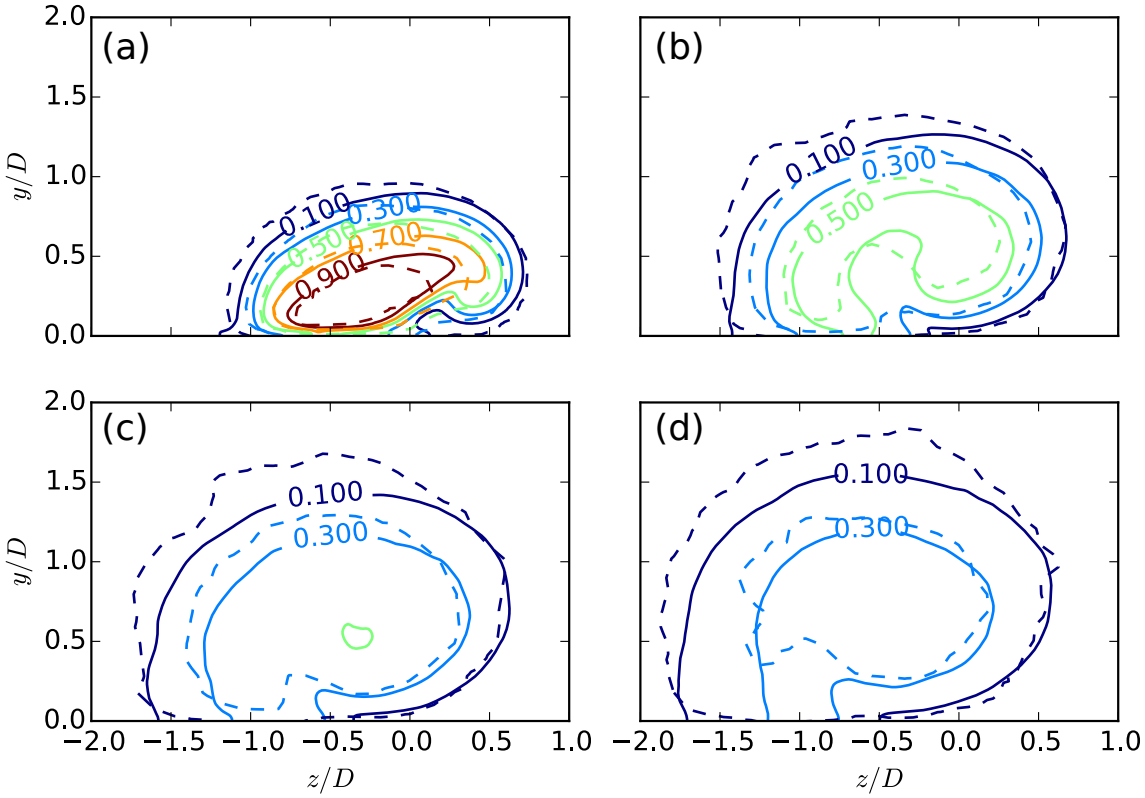

Figure 5.8 *Contours of the mean concentration. Planes are normal to streamwise direction at positions (a) $x = 1D$, (b) $x = 3D$, (c) $x = 5D$ and (d) $x = 7D$. Solid line is the passive scalar used in the simulation and dashed line is the contaminant used in the experiment.*

plane (a) the unity isocontour shows the similar shape that was observed inside the hole. The velocity is higher close to the leading edge than close to the trailing edge. Downstream the trailing edge the velocity of the flow is nearly zero thus the flow is detached from the wall. The velocity agreement between the simulation and the experiment is excellent close to the injection hole. Further away from the wall the velocity isocountours show a difference. Note that the isocontour comparison is very sensitive in the regions with small gradient thus even if the difference is relatively small, the resulting isocontour lines may be misaligned.

The passive scalar used in the present simulation and the contaminant used in the experiment are compared at the interaction region. Figure 5.8 shows the mean scalar and contaminant contours at four locations normal to streamwise direction: $x = 1D$, $3D$, $5D$ and $7D$. Figure 5.9 shows contours at three locations normal to wall direction: $y = 0.1D$, $0.5D$ and $0.9D$.

In the second plane in Figure 5.8(b) we can see the footprint of the CVP because the concentration is highest in the middle of the vortices. The vortex on the left side is smaller than on the right side and the CVP is tilted to the left. In Figure 5.9(a)

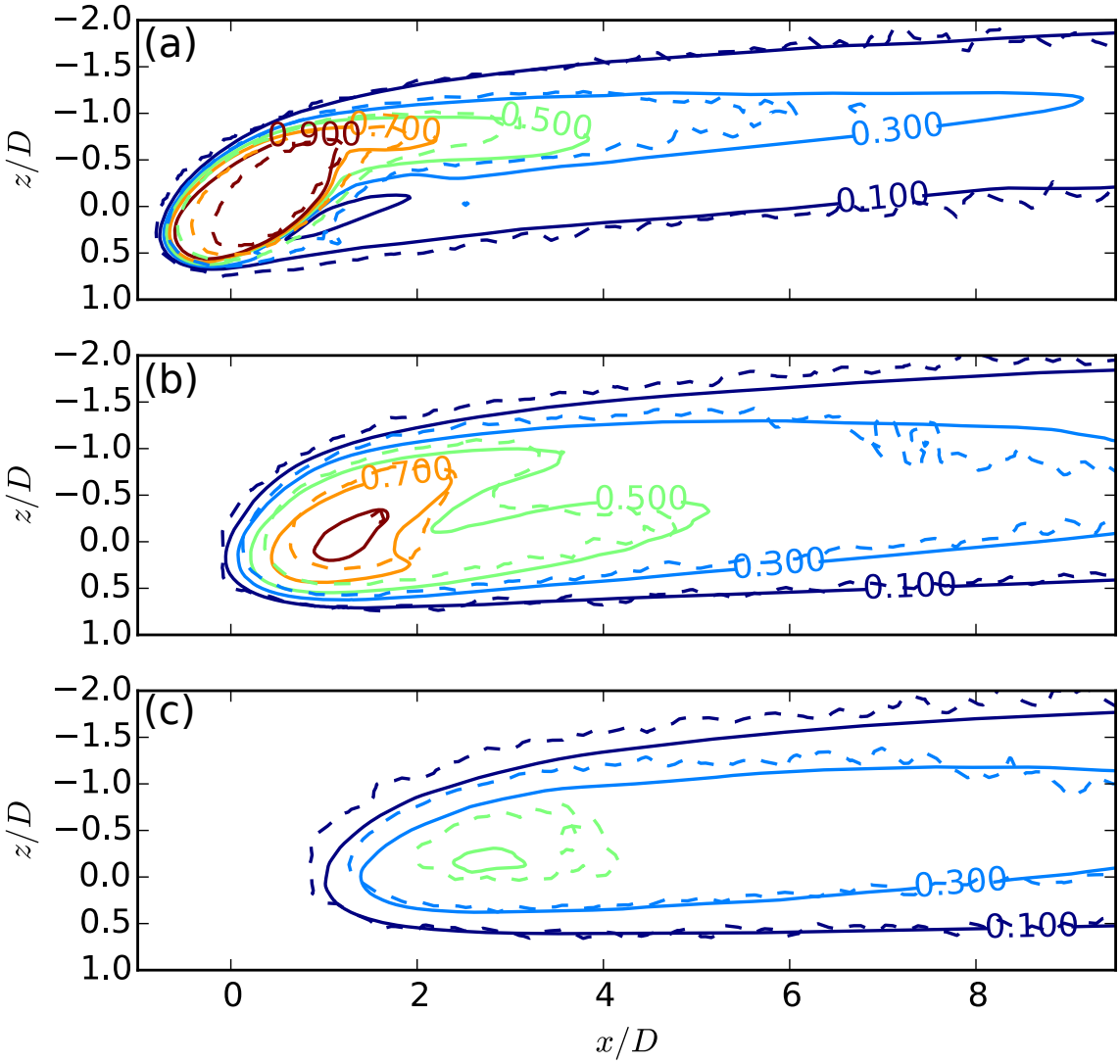

Figure 5.9 *Contours of the mean concentration. Planes are normal to wall direction at positions (a) $y = 0.1D$, (b) $y = 0.5D$ and (c) $y = 0.9D$. Solid line is the passive scalar used in the simulation and dashed line is the contaminant used in the experiment.*

the footprint of the smaller vortex is significant while the footprint of the bigger vortex is almost negligible which is a result of the tilt. Further from the wall in Figure 5.9(b) the sizes of the footprints are opposite, the leg of the stronger vortex (below) is longer than the leg of the smaller vortex (above). The contaminant is spread better than the momentum which can be determined by comparing the plane (c) in Figure 5.7 to plane (b) in Figure 5.9 which are at the same location $y = 0.5D$. The jet is detached and therefore the maximum concentration is not located at the wall which is consistent with the observations of Thole et al. [37].

Excellent agreement between the simulation and the experiment is achieved even though there is a big difference in the Schmidt numbers, namely 1 and 1500. This is a result of the large scale turbulent mixing dominating the molecular diffusion

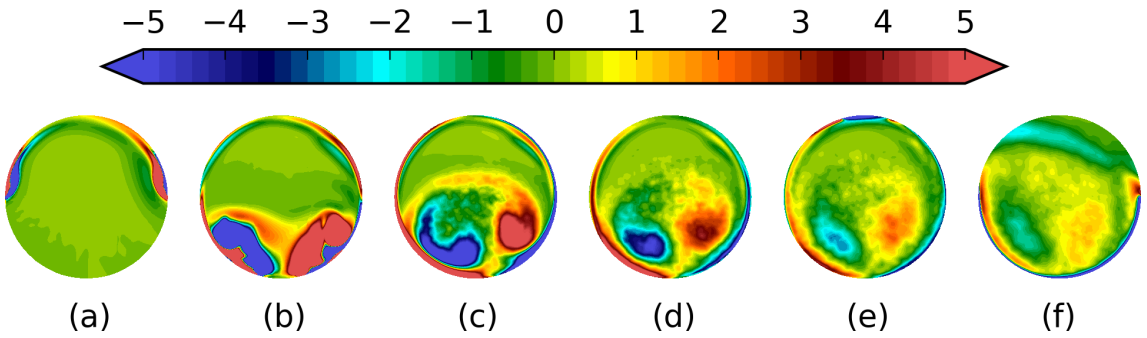

Figure 5.10 *The mean vorticity in hole axis direction inside the hole. The vorticity is normalized with D/U_{jet}. The cut plane locations are given in Figure 5.6.*

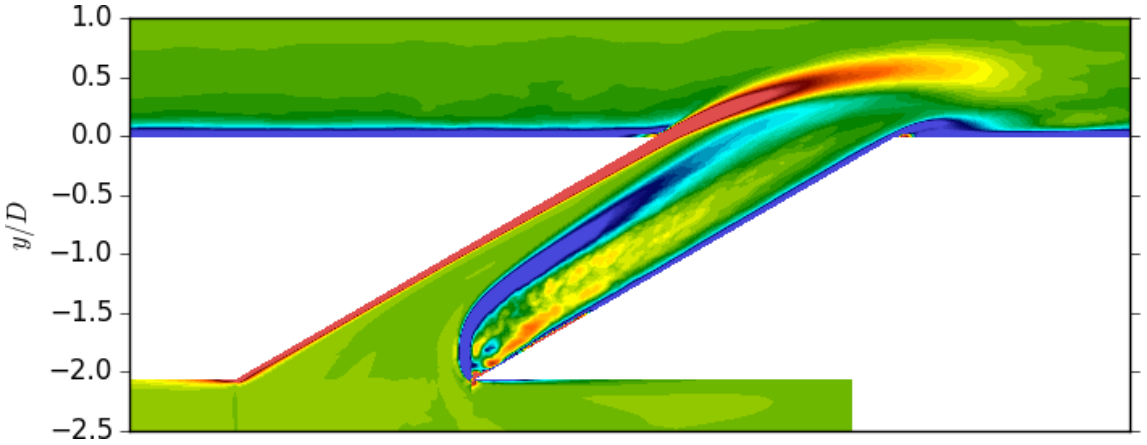

Figure 5.11 *The mean vorticity at the middle section of the hole. The vorticity is normalized with D/U_{jet}.*

of which the effect seems to be almost negligible. The concentrations show a small difference at the windward side of the injection which is consistent on all planes in Figure 5.8. The jet penetrates slightly better in experiment than in simulation which might be due to the difference in Schmidt numbers.

5.4 Mean vorticity

Let us now look at what coherent structures can be identified from the mean flow field by looking at the mean vorticity contours at various cut planes. Figure 5.10 shows the vorticity inside the jet hole. The vorticity is given in the axial direction and it is normalized with D/U_{jet}. The cut plane locations are given in Figure 5.6. The first plane (a) at the interface of plenum and hole shows the cross section of the elliptical shaped ring vortex. The ring vortex develops into a small counter-rotating vortex pair which is observed in the following planes (b)-(f). The flow is dominated with the vortex pair which loses its strength when moving downstream inside the hole.

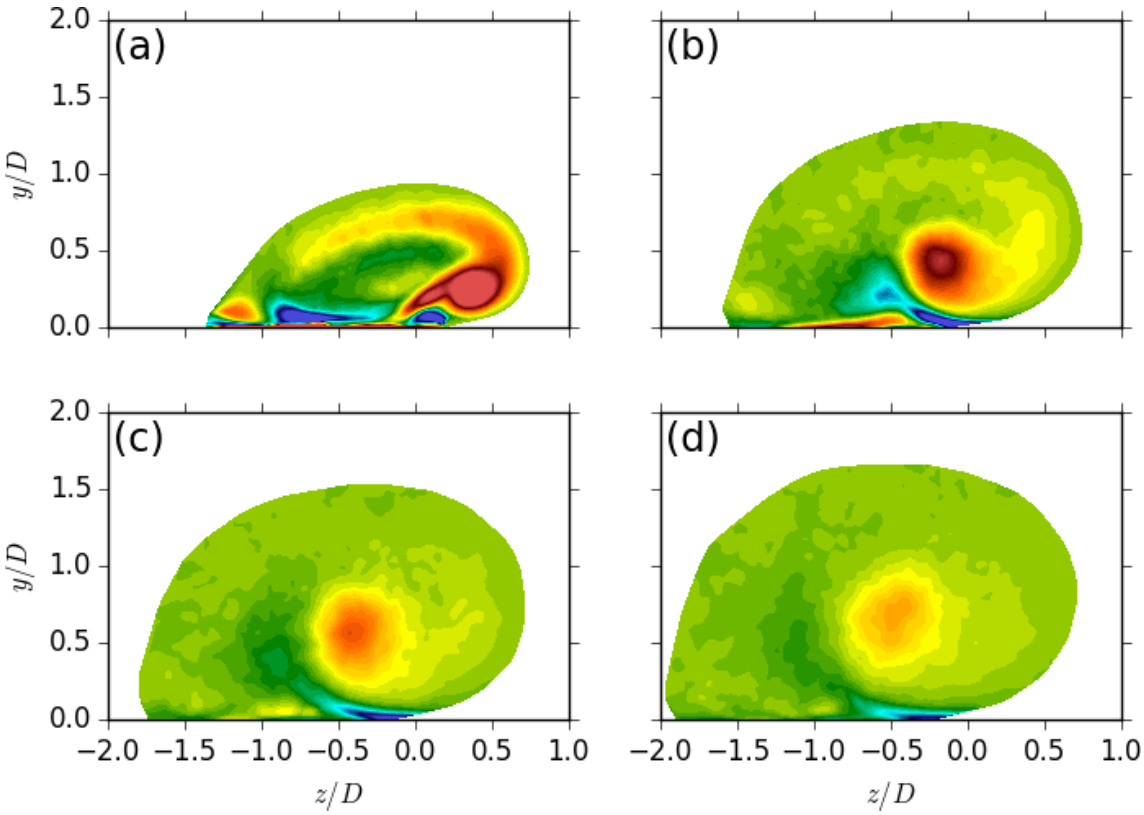

Figure 5.12 *Mean vorticity in streamwise direction at positions (a) $x = 1D$, (b) $x = 3D$, (c) $x = 5D$ and (d) $x = 7D$. The vorticity is normalized with D/U_{jet}.*

The middle section of the hole is shown in Figure 5.11. The vorticity is given in the plane normal direction which is $\mathbf{n} = \begin{bmatrix} 0.5 & 0 & 0.867 \end{bmatrix}^T$. Inside the hole a strong vorticity region (blue) is observed in the middle which is the shear layer between the two flows going to opposite directions (see Figure 5.5). At the hole exit the two boundary layers which have opposite vorticity signs encounter. The jet boundary layer vorticity dominates the crossflow boundary layer vorticity because only positive vorticity (red) is observed after the leading edge.

After the jet exit hole, the asymmetric CVP develops quickly and it is observed in Figure 5.12 which shows the streamwise vorticity on four planes normal to the streamwise direction. The planes show only the region where the mean scalar is $\overline{C} > 0.05$ to visualize the effect of the CVP to the shape of the jet. On the first plane (a) the vortices are rather far away from each other. The stronger vortex is off the wall at the edge of the jet while the weaker vortex is almost attached to the wall. A small opposite signed vortex is observed under the stronger vortex which unites with the weaker vortex of the CVP further downstream on plane (b) and the vortices of the CVP have moved closer to each other. Further downstream in planes (c) and (d) the CVP is diminished and the weaker vortex has almost disappeared. The center of the stronger vortex stalls approximately in the middle of the jet.

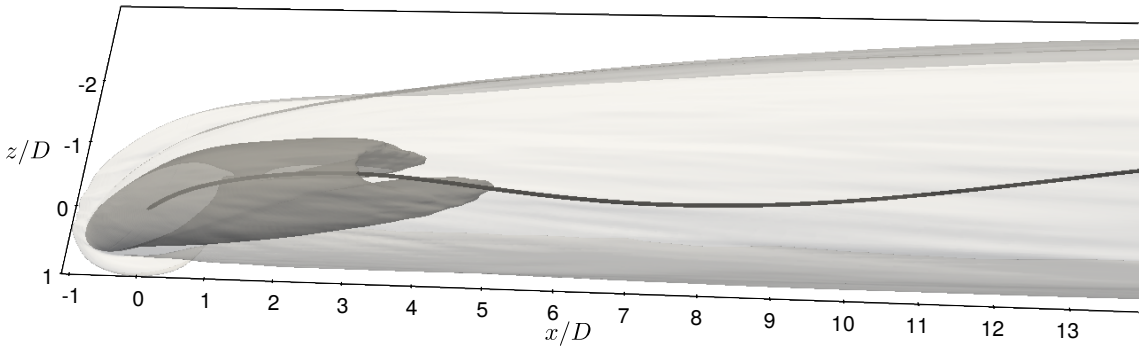

Figure 5.13 *Mean passive scalar concentration isocontours and jet trajectory. Light grey is* $C = 0.1$ *and dark grey is* $C = 0.5$.

5.5 Entrainment

Entrainment characterizes the mixing of the jet and the crossflow. The higher entrainment means that the jet spreads and penetrates better to the crossflow. It is well known that a transverse jet entrains better than a regular free jet to the surrounding fluid [44]. However, the entrainment of an inclined jet is not necessarily better than for the regular free jet [8]. A common way to measure the entrainment of a jet is to calculate the volume flux through the jet cross sections which is given by

$$\dot{V}_s = \int_{A_s} U_s \, dA_s, \tag{5.4}$$

where A_s is the area of the jet cross section and U_s is the velocity normal to the jet cross section. The jet cross sections are defined as planes normal to the jet trajectory delimited by a low scalar value. An unambiguous way to choose the jet trajectory is the streamline originating from the center of the jet exit hole. Such a jet trajectory and two scalar isocontours of the present simulation are shown in Figure 5.13.

The entrainment is calculated for the present asymmetric jet in crossflow and for a symmetric jet in crossflow investigated by Bodart et al [4]. The latter configuration does not include any compound angle but the other characteristics such as the velocity ratio, crossflow boundary layer, injection angle and jet hole length are comparable to the present jet in crossflow. The scalar delimiter value is chosen for both jets in crossflow to $C = 0.01$ which is shown to represent fairly the entrainment characteristics [26].

The entrainment and the area of the jet cross sections are given in Figure 5.14. Solid line is the present asymmetric jet, dashed line is the symmetric jet and point line is Ricou-Spalding correlation for a regular free jet [32]. The present asymmetric jet entrains always better than the symmetric jet. The entrainment increases more

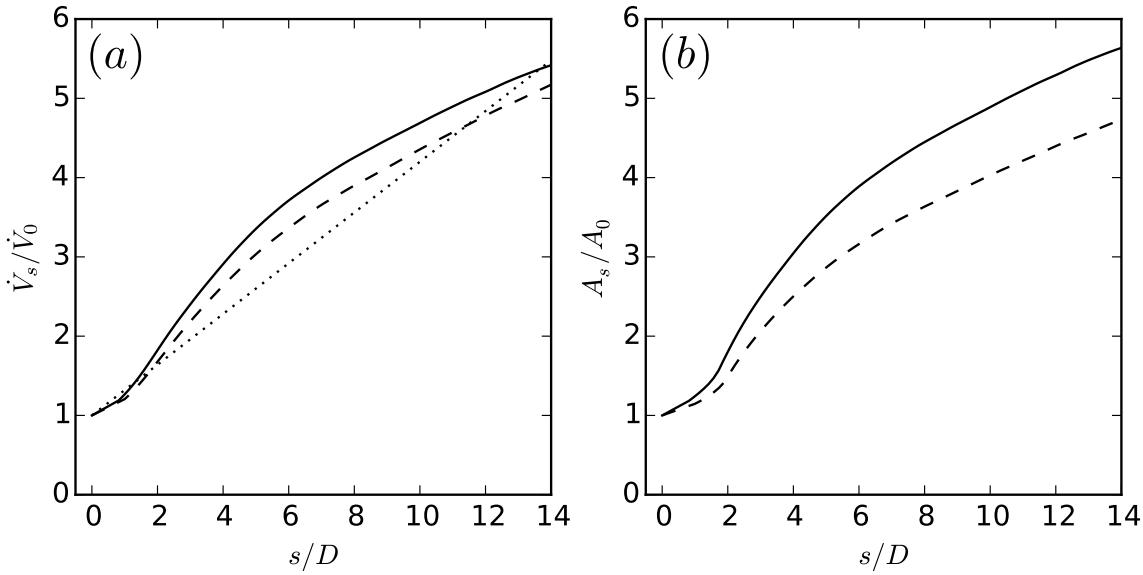

Figure 5.14 *(a) Entrainment of the jet and (b) evolution of the jet cross section. The values are normalized with the initial values at the jet exit V_0 and A_0. s is the streamline length from the jet exit. Solid line is the present simulation, dashed line is symmetric jet by Bodart et al. [4] and point line is Ricou-Spalding correlation [32] for the regular axisymmetric jet.*

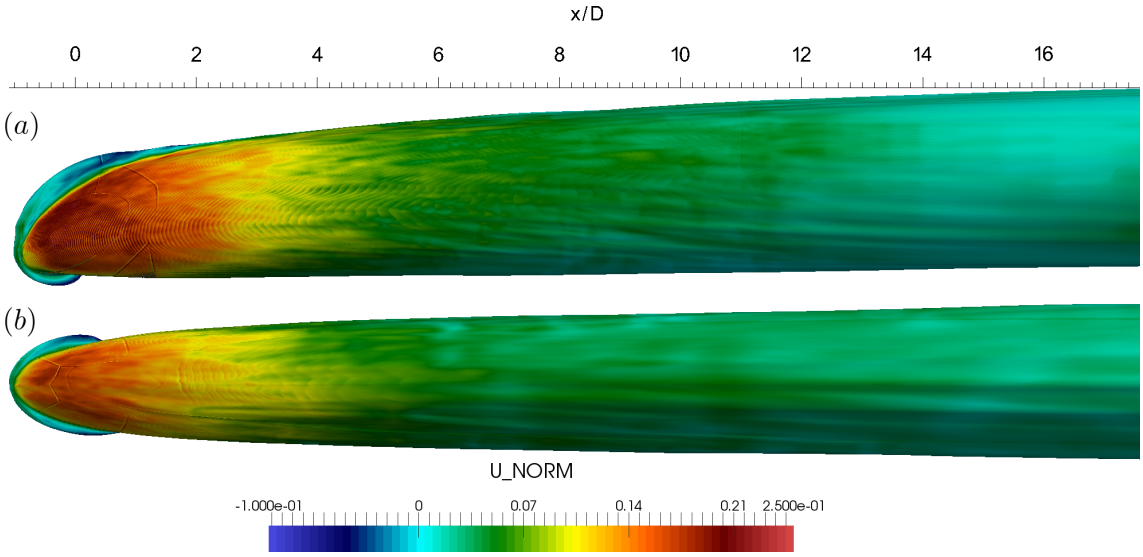

Figure 5.15 *Top view of the mean passive scalar concentration isocontour $C = 0.1$ and the mean velocity normal to the isocontour. (a) the present asymmetric jet and (b) the symmetric jet by Bodart et al. [4].*

rapidly for the asymmetric than for the symmetric jet until $s = 7D$. Thereafter, the entrainment rate remains approximately the same. Figure 5.14(b) shows that the higher entrainment is due to the better spreading of the asymmetric jet. The difference in areas is greater than in the entrainment and therefore the average velocity through the surface is lower for the asymmetric jet. The lower velocity corresponds to lower penetration and results that the jet is spread closer to the wall. This is highly desirable property for a film cooling configuration because it increases the film cooling efficiency.

Figure 5.15 shows the mean velocity normal to the mean scalar concentration iso-contour. Therefore, it identifies regions of the jet in which fluid is "crossing" its boundary and localize where the entrainment occurs. From this figure, it is shown that most of the entrainment occurs in the shear layer between the jet and the cross-flow in which the large scale jet shear layer vortices are observed. However, some differences can be observed between the two configurations: the compound angle injection of the asymmetric jet (above) increases the size of the interface region between the jet and the crossflow near the jet exit hole which results into higher entrainment especially to the negative z side (above).

The entrainment of the regular jet is higher shortly after the injection than for the jets in crossflow while after respectively $1.5D$ and $2D$ for the asymmetric and the symmetric jet the entrainment becomes higher. Muppidi and Mahesh [26] show that in the far field the major part (> 80 %) of the entrainment occurs on the leeward side for their transverse jet in crossflow with high velocity ratio ($r = 5.7$). Consequently, for the inclined jets in crossflow with low velocity ratios the wall prevents the jet entraining on the leeward side [8].

5.6 Turbulence quantities

The turbulence kinetic energy k is a measure of the level of turbulent agitation and therefore it is an important quantity to characterize a turbulent flow. Moreover, in the RANS framework the closure of the system of equation usually requires to solve a transport equation for the turbulence kinetic energy along with another turbulence quantity. Figure 5.16 shows the turbulence kinetic energy localized in the middle plane of the hole $\mathbf{n} = \begin{bmatrix} 0.5 & 0 & 0.867 \end{bmatrix}^T$. The peak of turbulence kinetic energy is located right after the junction at the bottom of the hole where the separation occurs. The turbulent kinetic energy is high at the middle of the cross section and follows the shear layer inside the hole. After the jet exit the interaction with the boundary layer creates another shear layer and localize the most of the turbulent

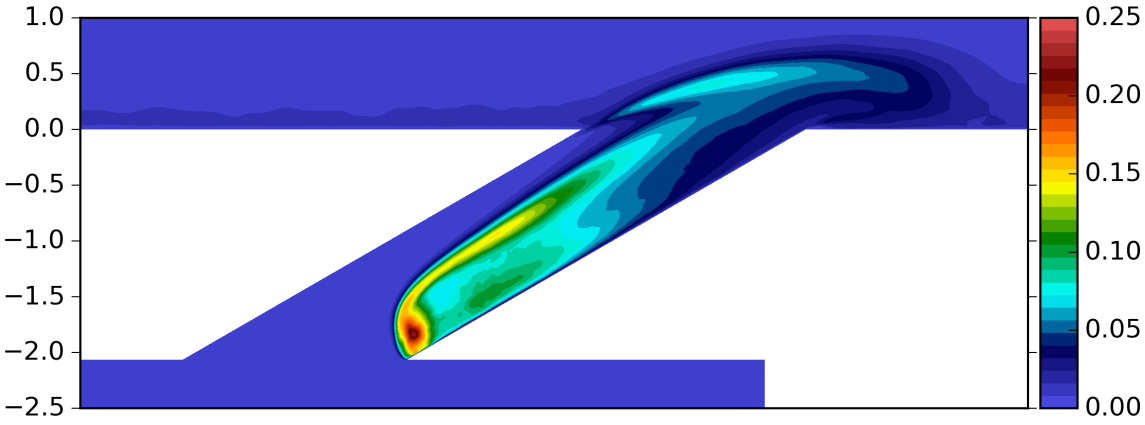

Figure 5.16 *Turbulence kinetic energy the middle section of the hole. The turbulence kinetic energy is normalized with* U_{jet}^2.

.

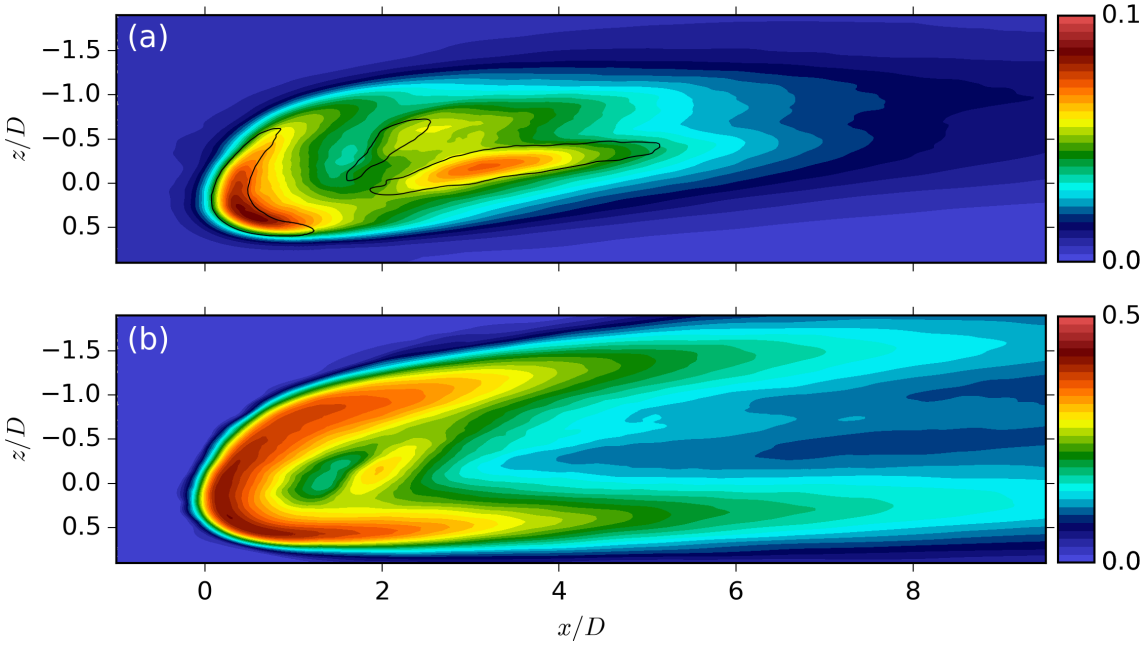

Figure 5.17 *(a) Contours of turbulence kinetic energy and isocontour line of vorticity magnitude* $\omega_{mag} = 1.5\,U_{jet}/D$ *and (b) RMS of the passive scalar on plane normal to wall direction at* $y = 0.5D$. *The turbulence kinetic energy is normalized with* U_{jet}^2.

.

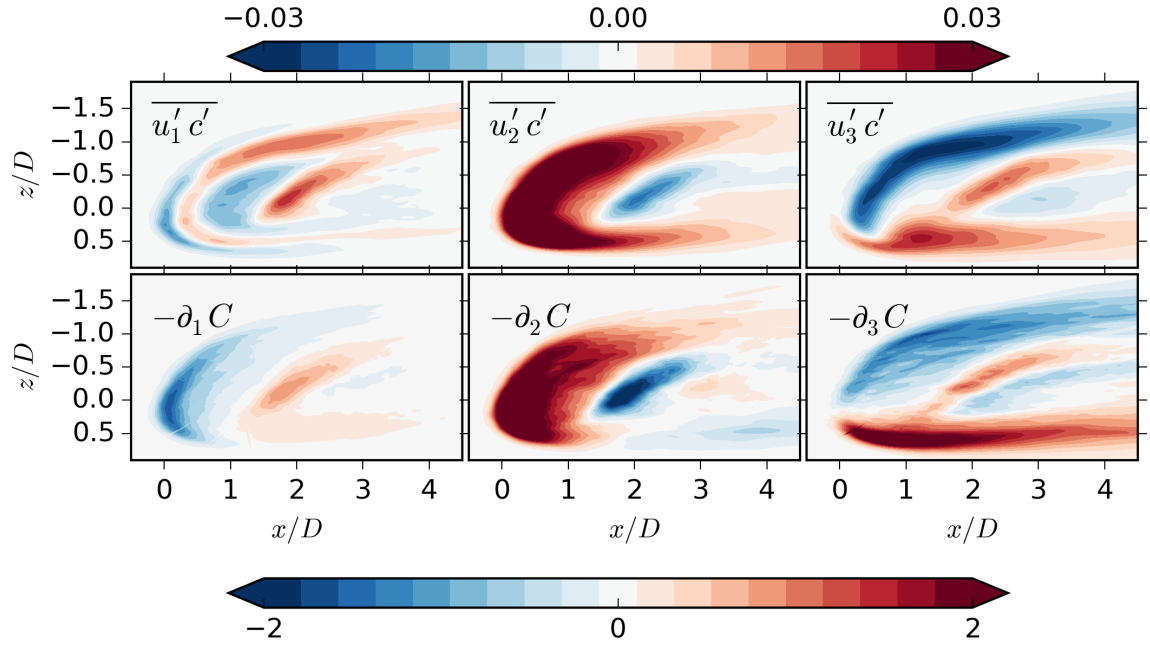

Figure 5.18 *Turbulent scalar flux $\overline{u_i' c'}$ and the mean scalar gradient on plane normal to wall direction at $y = 0.5D$. Colourbar above is for scalar flux and below is for mean scalar gradient. The turbulent scalar flux is normalized with U_{jet} and the gradient with $1/D$.*

kinetic energy on the windward side of the jet.

Figure 5.17(a) shows contours of the turbulence kinetic energy and an isocontour of vorticity magnitude on a wall normal plane at $y = 0.5D$. Two red peaks are observed and localize the most of the turbulent kinetic energy production. The two peaks coincide with vorticity isocontour. Starting from the left, the first peak is in the region of the jet shear layer vortices and the other is the region of the stronger vortex of the CVP. Figure 5.17(b) shows the root mean square (RMS) of the passive scalar on the same plane. The highest intensity is found at the windward side interface between the jet and the crossflow. The scalar RMS contour is rather symmetric in the spanwise direction in comparison to the turbulent kinetic energy. Note that while the mean scalar concentration agreement is excellent between the simulation and the experiment, the scalar RMS would probably diverge significantly because of the large difference in Schmidt numbers.

5.7 Turbulent scalar flux

Turbulent scalar flux $\overline{u_i' c'}$ is the unknown that arises from the Reynolds-averaged transport equation for the passive scalar (3.16) and has to be modelled to close the system of RANS equations. Similarly to the Reynolds stress tensor, an easy way to model scalar flux is to use the standard gradient diffusion hypothesis (SGDH)

which assumes that the scalar flux is aligned with the mean scalar gradient (Equation (3.19)) thus assuming a single component and constant eddy diffusivity. From LES the turbulent scalar flux and the mean scalar gradient can be directly calculated in order to benchmark the SGDH. The validity of the SGDH has been previously investigated for a transverse jet [26] and a symmetric jet in crossflow [4]. Not surprisingly, the results strongly diverge from the simple hypothesis in some regions where even counter-gradient diffusion is observed. The scalar flux alignment has been shown to be dependent on the mean shear in addition to the mean scalar gradient [33] and therefore in the regions of strong shear the orientation of the scalar flux and the scalar gradient may be very different.

Figure 5.18 shows the results for the present asymmetric jet in crossflow configuration. For simplicity the turbulent scalar flux and the mean scalar gradient are given in a plane normal to the wall direction at $y = 0.5D$. The figure shows that most of the high concentration gradients are roughly located in the region of the highest scalar flux. However, two regions with counter-gradient diffusion are observed. First, the x-component of scalar flux exhibits a positive region between negative regions close to the leading edge which is not correlated with the scalar gradient. This region coincides with the region of the jet shear layer vortices which is consistent with the observations of Béguier and Fulachier [3] who show in their shear flow with asymmetric scalar distribution that counter-gradient diffusion occurs in the regions with large scale structures. Another region is observed on the y-component of the scalar flux for positive z. The scalar flux remains positive while the gradient changes from positive to negative.

The evolution of the scalar flux can be studied by analysing its transport equation. This equation can be obtained from the momentum Equation (3.3) by multiplying it with passive scalar and then Reynolds averaging the product. The transport equation can be written as follows

$$\frac{\partial \overline{u_i' c'}}{\partial t} + A_i = - P_i - \epsilon_i - T_i - \Phi_i, \tag{5.5}$$

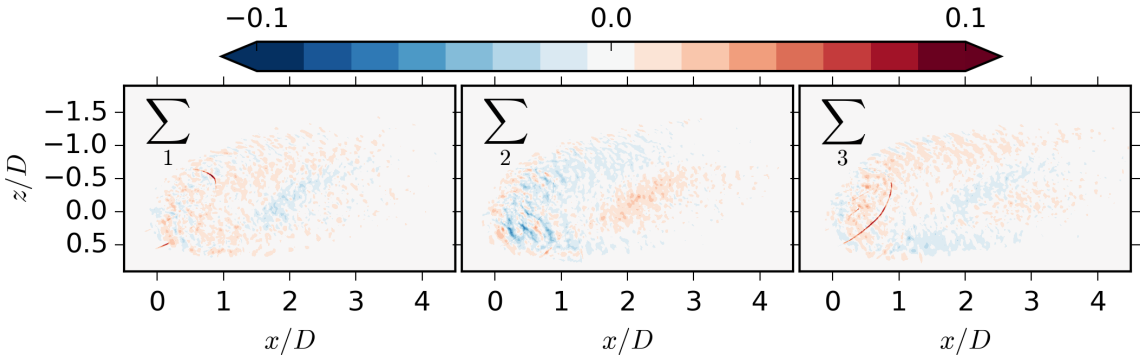

Figure 5.19 *Sum of the terms in Equation (5.5) on plane normal to wall direction at* $y = 0.5D$*. The terms are normalized with* D/U_{jet}^2*.*

in which the terms are from left to right

$$\begin{aligned}
\text{Advection} \quad A_i &= U_j \frac{\partial(\overline{u_i' c'})}{\partial x_j} \\
\text{Production} \quad P_i &= \overline{u_j' u_i'} \frac{\partial C}{\partial x_j} + \overline{u_j' c'} \frac{\partial U_i}{\partial x_j} = P_i^C + P_i^U \\
\text{Dissipation} \quad \epsilon_i &= (\mathcal{D} + \nu) \overline{\frac{\partial c'}{\partial x_j} \frac{\partial u_i'}{\partial x_j}} \\
\text{Transport} \quad T_i &= \frac{\partial}{\partial x_j} \left(\overline{u_j' u_i' c'} + \frac{\overline{p' c'}}{\rho} \delta_{ij} \right) \\
\text{Pressure scrambling} \quad \Phi_i &= \overline{\frac{p'}{\rho} \frac{\partial c'}{\partial x_i}}.
\end{aligned}$$

The time-dependent term is neglected because of the statistically steady state assumption in the present case. The scalar flux $\overline{u_i' c'}$ is calculated during the simulation thus the advection and production terms can be directly evaluated. The rest of the terms are extracted from 1030 instantaneous snapshots which are generated during the simulation. The files contain the instantaneous fields of primitive variables p, u, T and c. Each file is around 13 GB in size and the files are written in every 0.23 time units $T = D/U_{jet}^2$.

The level of convergence is estimated by summing up all the terms in Equation (5.5). Figure 5.19 shows the result which should approach zero amplitude everywhere for a perfectly converged simulation. The planes show regions of divergence (red and blue spots) and an obvious reason is the relatively low number of samples for the second and third order terms which are not fully converged statistically. Another reason may come from the gradient computation by the post-processing tool. In particular, the mesh effects on the gradient computation which is seen as a thin red line close to the jet exit hole. Better convergence could be achieved by increasing the number of samples and by calculating the gradients with more sophisticated scheme during

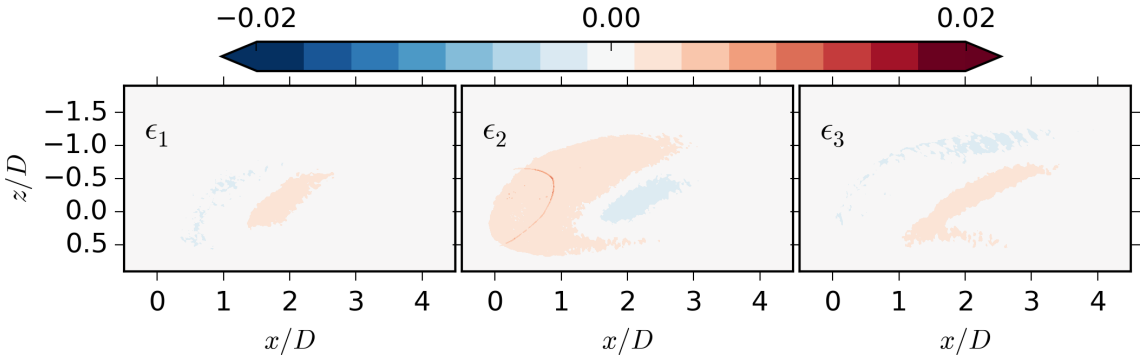

Figure 5.20 *Dissipation on plane normal to wall at $y = 0.5D$. The terms are non-dimensionalized with D/U_{jet}^2.*

the simulation. In this work, due to the moderate level of convergence we focus on a qualitative interpretation of these terms. We show in Figure 5.19 that the level of convergence is satisfactory when compared to the magnitude of the terms in Figure 5.21.

According to Overhalt and Pope [27] the ratio of dissipation to production becomes negligible at high Reynolds number flows and the scalar flux is destroyed solely by the pressure scrambling term Φ_i. Figure 5.20 shows the dissipation in the present simulation. Note that the scale factor is five times smaller than in the Figure 5.21. Thus the dissipation is considerably smaller than the other terms in the transport equation and is neglected in the following analysis.

In Figure 5.21 the significant terms of Equation (5.5) are given on a plane normal to wall direction at $y = 0.5D$. The three columns are from left to right respectively streamwise, spanwise and wall normal components and the terms are normalized with D/U_{jet}. These terms may be interpreted as follow, from top to bottom. The advection term A_i and the turbulence transport term T_i represent respectively the transport of scalar flux by the mean flow and the turbulence fluctuations. The turbulence tends to homogeneity and therefore the turbulence transport term transfers the scalar flux from higher to lower magnitude regions. The production term P_i is the generation of scalar flux by the interaction with the mean field of velocity and the mean scalar concentration. The pressure scrambling term Φ_i is the fluctuating pressure scalar gradient correlation term. It is responsible for the destruction of the turbulent scalar flux.

Veeravalli and Warhaft [39] showed that advection and transport terms and production and pressure terms approximately balance each other in the context of a shearless mixing layer. This seems consistent in the present simulation for the production and pressure terms $P_i \sim -\Phi_i$. However, the advection and transport terms

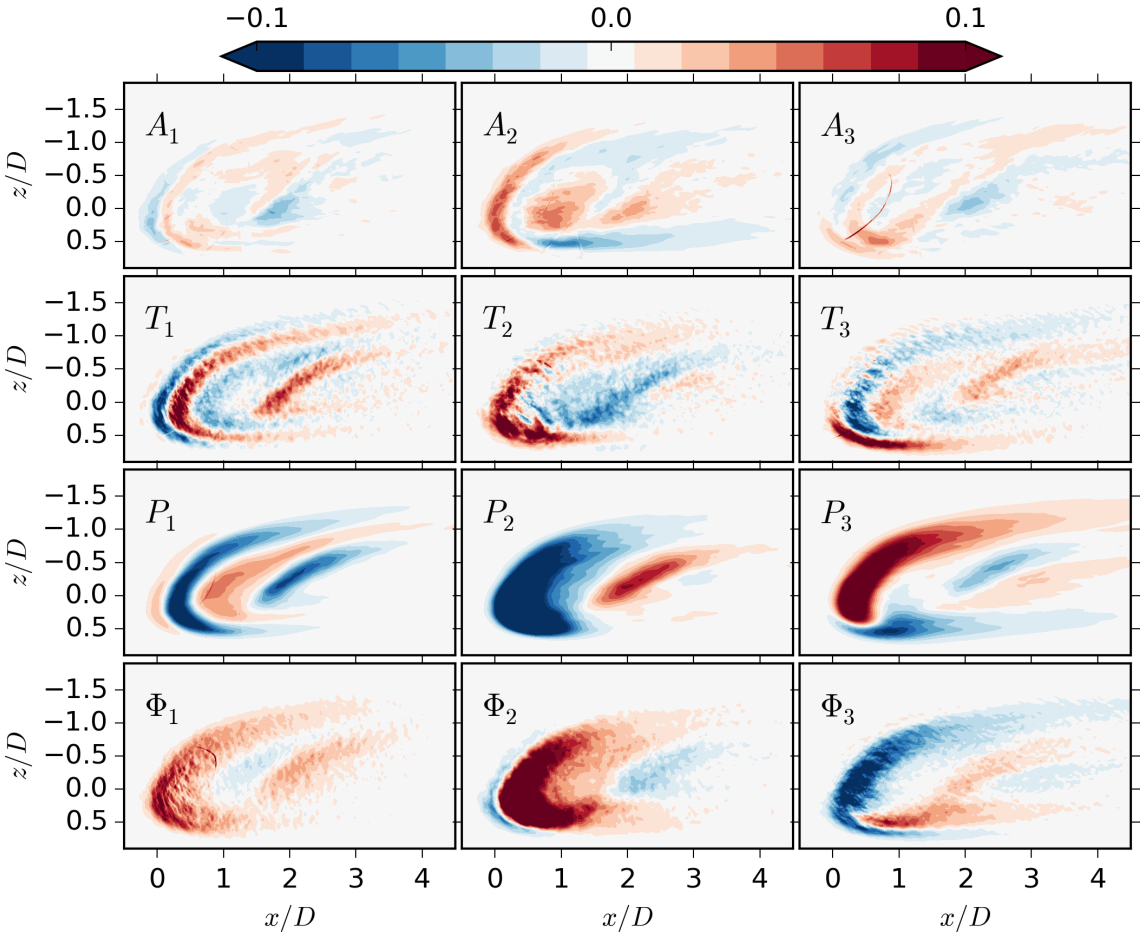

Figure 5.21 *Significant terms in Equation (5.5) on plane normal to wall direction at $y = 0.5D$. The terms are non-dimensionalized with D/U_{jet}^2.*

are quite different. The signs are opposite in the core region but identical close to the interface between the jet and the crossflow. Additionally, the advection term is weaker than the other significant terms.

Production

The two production subterms denoted P_i^C and P_i^U are shown in Figure 5.22. The complete decomposition of the terms is respectively given in Figure 5.23 and Figure 5.24. These two terms differ strongly by nature. We see in Figure 5.23 that the first production term is mainly diagonal and always acts in the mean scalar gradient direction. This is consistent with the gradient diffusion hypothesis: velocity fluctuations aligned with a concentration gradient tend to produce a scalar flux aligned in the same direction.

The second term P_i^U is the result of the interaction of the scalar flux with the mean shear what can be identified as an induced flux and support a statistical reasoning.

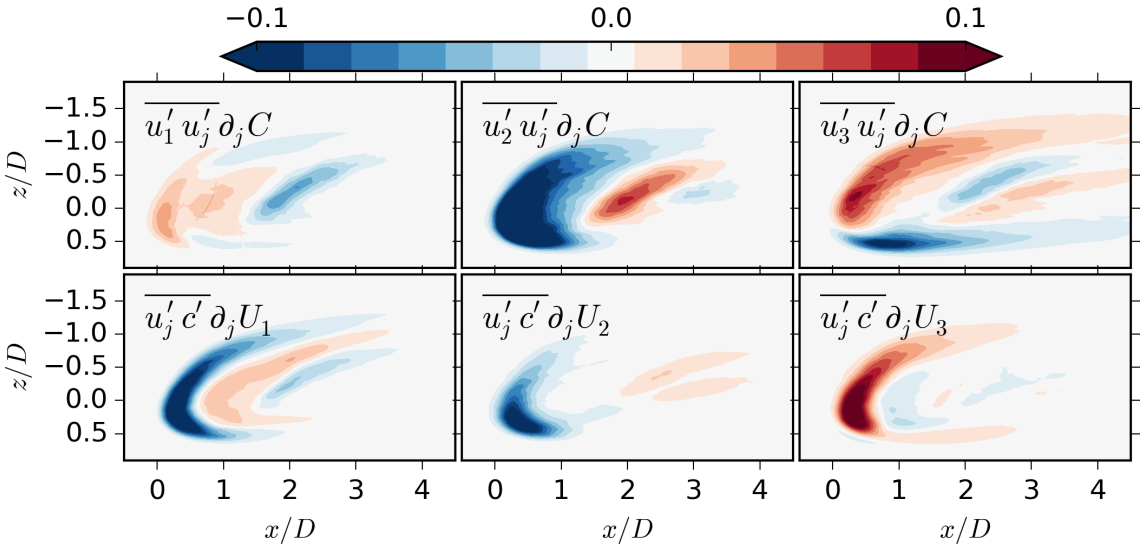

Figure 5.22 *Production terms P_i^C and P_i^U on plane normal to wall direction at $y = 0.5D$. The terms are non-dimensionalized with D/U_{jet}^2.*

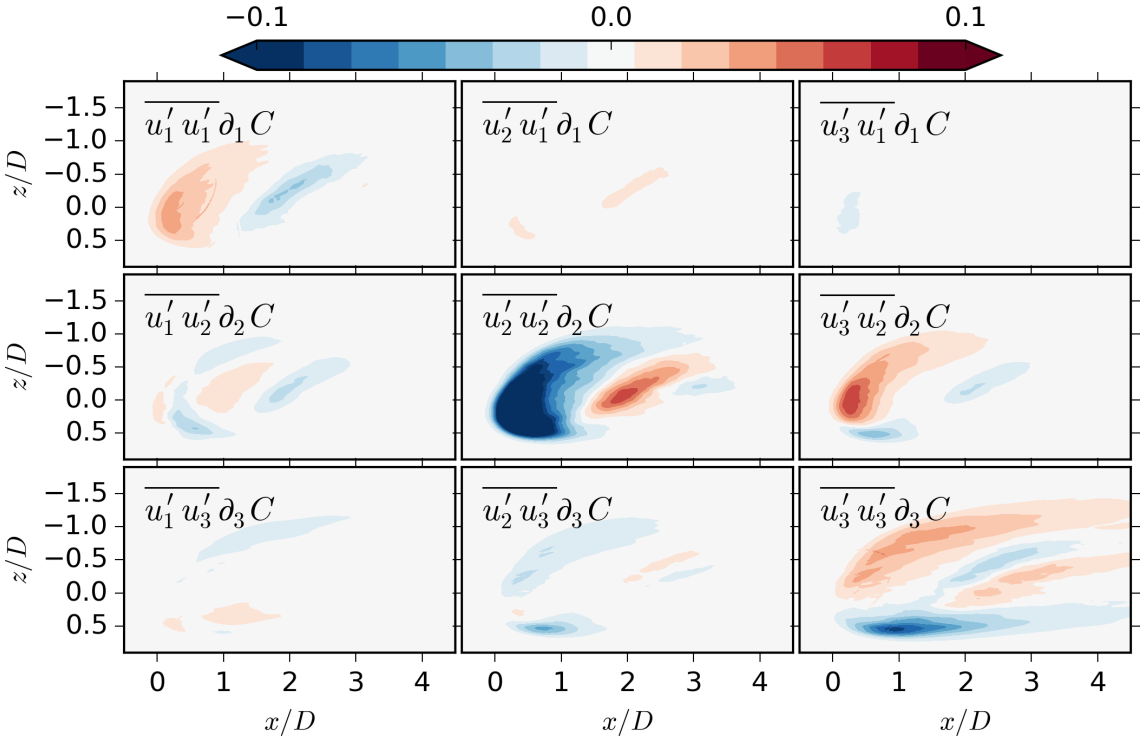

Figure 5.23 *Decomposition of the production term P_i^C on plane normal to wall direction at $y = 0.5D$. The terms are non-dimensionalized with D/U_{jet}^2.*

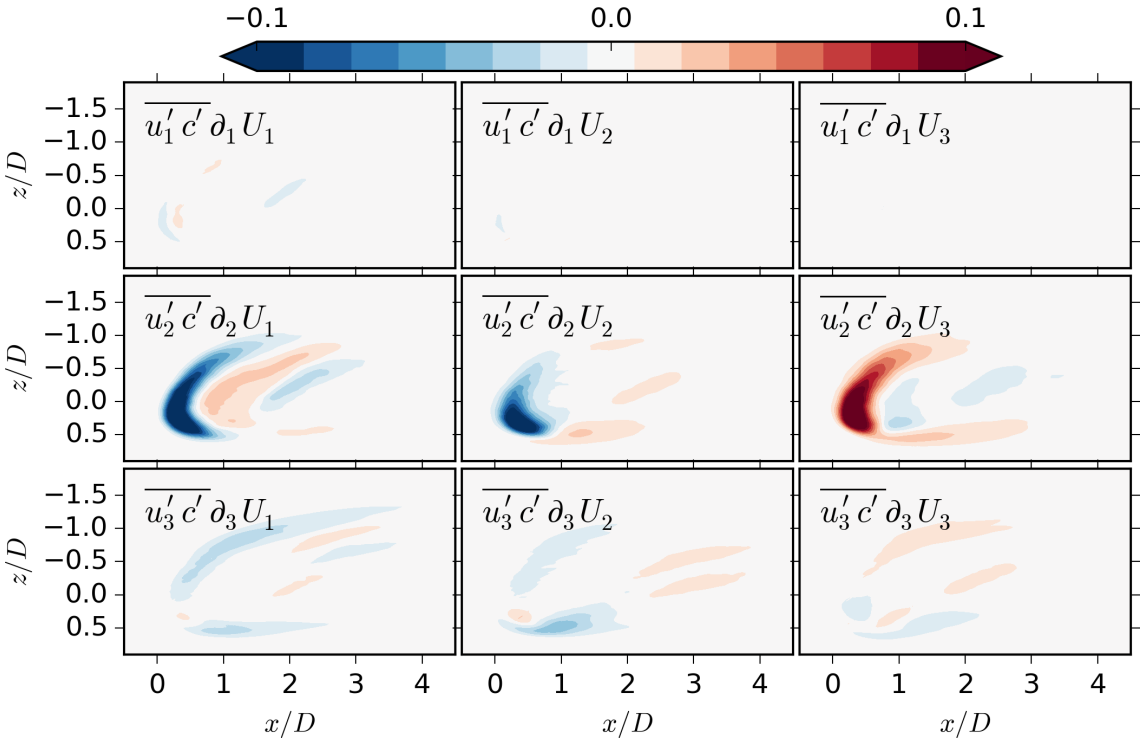

Figure 5.24 *Decomposition of the production term P_i^U on plane normal to wall direction at $y = 0.5D$. The terms are non-dimensionalized with D/U_{jet}^2.*

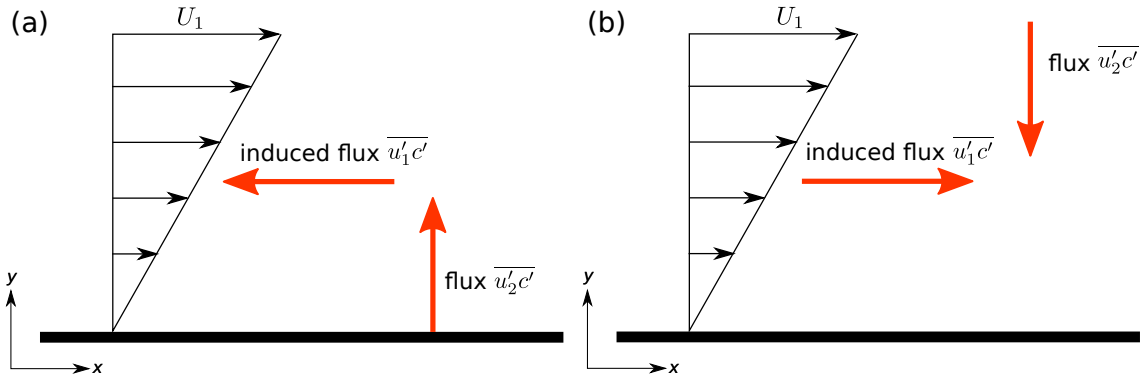

Figure 5.25 *Description of the induced flux occurring in the interaction of a concentration gradient and a mean shear in the y-direction. Mean scalar gradient in (a) negative and (b) positive y-direction.*

Figure 5.25 shows an example of such an induced flux in a shear flow. In this example, we assume a positive mean shear gradient in the y-direction. Following a gradient type hypothesis, we assume an initial scalar flux is produced in the direction of a scalar concentration gradient. In plane (a) the positive fluctuations u_2' are associated with positive c' and negative u_2' with negative c'. The mean shear associates positive u_2' with negative u_1' and negative u_2' with positive u_1'. Consequently, if u_2' is positive then c' is positive and u_1' is negative which is consistent with $\overline{u_1' c'} \sim -\overline{u_2' c'} \frac{\partial U_1}{\partial x_2}$. This induced flux can easily create counter gradient diffusion,

depending on the relative alignment of the mean shear and the concentration gradient. This is consistent also for a scalar flux coming from an opposite y-direction in Figure 5.25(b).

5.8 Algebraic turbulent scalar flux models

The SGDH assumes isotropic behaviour and that the turbulent scalar flux is aligned with the mean scalar gradient. The previous section showed counter-gradient diffusion regions in which the scalar flux and the scalar gradient are completely misaligned. We present some of the most common algebraic turbulent scalar flux models which aims at improving the accuracy. Daly and Harlow [9] formed an extension to the SGDH which allows some anisotropy. This generalized gradient diffusion hypothesis (GGDH) is given by

$$\overline{u_i'c'} = -C_\theta \tau \overline{u_i'u_j'} \frac{\partial C}{\partial x_j}, \tag{5.6}$$

where C_θ is a model constant and τ is a time scale. The time scale is usually taken as the turbulent time scale given by

$$\tau = \frac{k}{\epsilon}, \tag{5.7}$$

where $\epsilon = \nu \overline{\frac{\partial u_i'}{\partial x_k} \frac{\partial u_i'}{\partial x_k}}$ is the dissipation rate of turbulence kinetic energy. Note that the GGDH is simply the production term P_i^C multiplied by a time scale and a constant. A more recent extension to the GGDH is the high-order gradient diffusion hypothesis (HOGGDH) by Abe and Suga [1] which is given by

$$\overline{u_i'c'} = -C_\theta \tau \left(\frac{\overline{u_i'u_k'}\,\overline{u_k'u_j'}}{k} \right) \frac{\partial C}{\partial x_j}. \tag{5.8}$$

The HOGGDH uses a quadratic form of the Reynolds stress and therefore allows more anisotropy than the GGDH. Another obvious extension to the GGDH is the WET model by Launder [22] which is given by

$$\overline{u_i'c'} = -C_\theta \tau \left(\overline{u_i'u_j'} \frac{\partial C}{\partial x_j} + \overline{u_j'c'} \frac{\partial U_i}{\partial x_j} \right). \tag{5.9}$$

The WET model uses both of the production terms P_i^C and P_i^U.

The modelled turbulent scalar fluxes are evaluated with the four models (SGDH, GGDH, HOGGDH, WET) and compared with the present LES. The WET model

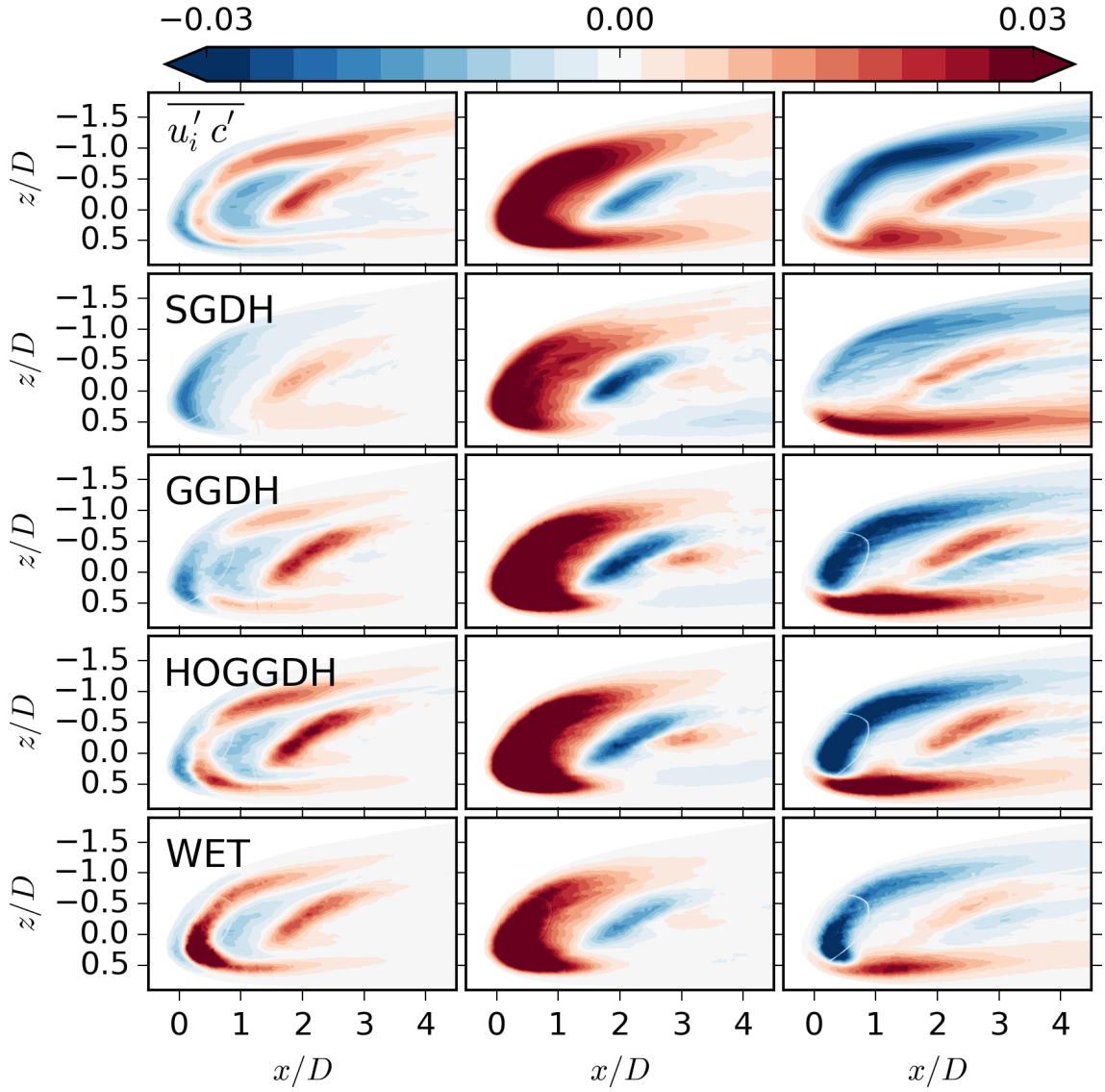

Figure 5.26 *Turbulent scalar flux models on plane normal to wall direction at $y = 0.5D$. The terms are non-dimensionalized with D/U_{jet}.*

is implicit in the scalar flux and therefore a least square method is used to solve the Equation (5.9). The model constants were determined by using a trial and error procedure. The turbulent diffusivity used in SGDH is set to $\mathcal{D}_t = 0.01$ and the model constants are set to $C_\theta = 0.1$, 0.1 and 0.05 respectively for GGDH, HOGGDH and WET. Figure 5.26 shows the results. The first row is the turbulent scalar flux extracted from the present LES results for comparison and the following rows are respectively SGDH, GGDH, HOGGDH and WET. The angles between the scalar flux calculated with models and present LES are given in Figure 5.27. Note that in RANS computations the Reynolds stresses $\overline{u_i'u_j'}$ are also modelled and therefore induce an additional modelling error for the momentum field which also affects the modelling of the turbulent scalar flux. Here we know the velocity field *a priori* and thus we will isolate the error produced by the turbulent scalar flux modelling only.

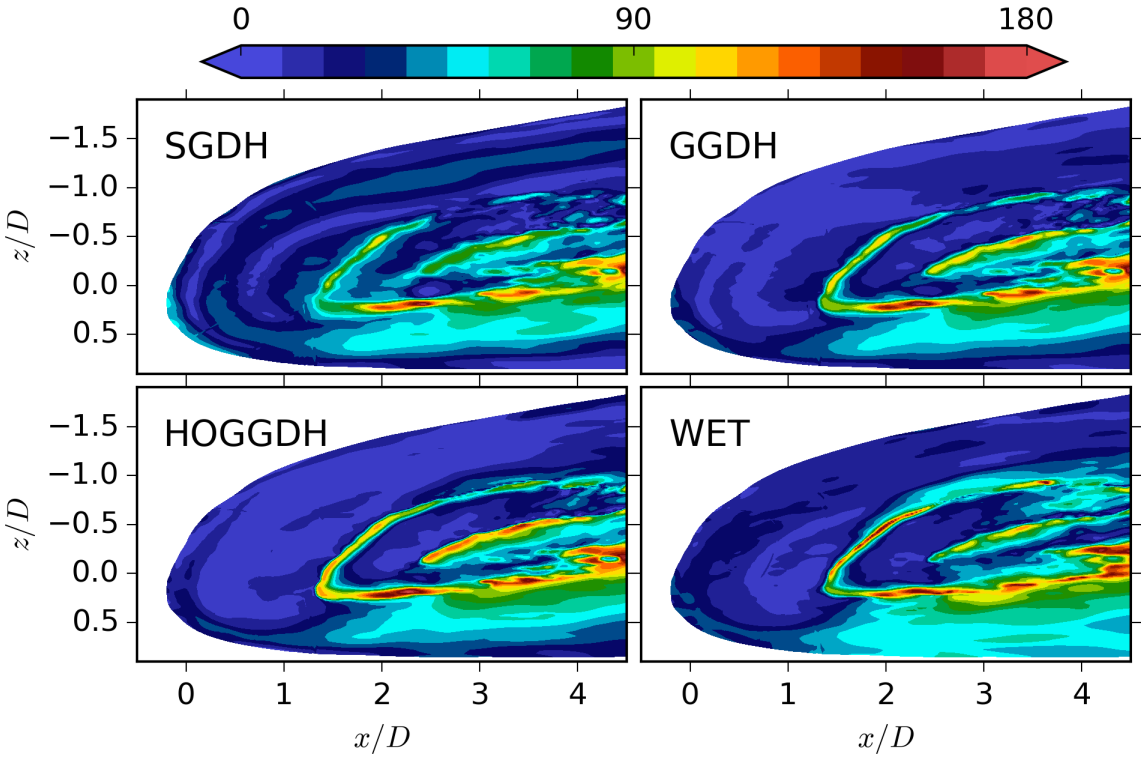

Figure 5.27 *Angle between the scalar flux model and turbulent scalar flux on plane normal to wall direction at* $y = 0.5D$.

As expected from the previous section the GGDH is only capable of capturing a small part of the counter-gradient diffusion regions because the P_i^C follows approximately the sign of the mean scalar gradient. The HOGGDH improves the accuracy in streamwise component in comparison to GGDH but the counter-gradient diffusion region is still too weak. However, in the WET model the other production term P_i^U is also included and therefore the counter-gradient region in streamwise direction is well exhibited. These two production terms correspond to different physical mechanisms as was pointed out in the previous section and therefore the results could be improved by using two different time scales. The results suggest that the first production term P_i^C is involved with larger time scales and P_i^U with shorter time scales.

The streamwise and wall normal components do not show much difference between the three extended SGDH models (GGDH, WET and HOGGDH). None of the models is capable of capturing the counter-gradient diffusion region in the spanwise direction at $z = 0.5D$ and therefore the greatest misalignment region in angle is there. The peak angles are observed on line regions in which both the turbulent scalar flux by LES and models are very weak. Consequently, the net effect of these regions may be negligible. Note that for more precise comparison the model coefficients should be optimized and the constant should be divided in two for the WET model.

6. CONCLUSIONS

A high fidelity large eddy simulation of an asymmetric jet in crossflow was performed to study the passive scalar mixing. The configuration includes the most relevant physics of a film cooling application. The jet is both inclined and skewed 30 degrees making the configuration asymmetric in the spanwise direction. The velocity ratio is unity between the jet and the crossflow. Particularly, extra caution was taken to represent the inflow boundary conditions. A synthetic turbulence generator is used for the approaching crossflow boundary layer and the jet feeding plenum is included to the domain to capture the complex flow phenomenon inside the short hole before the interaction.

The mean flow field was compared with an experiment by Ryan et al. [34] which has exactly the same geometry. In the simulation, the Reynolds number is two times higher and the Schmidt number is 1500 times lower than in the experiment. Nevertheless, the agreement is excellent for the mean velocity and the mean scalar concentration. The latter is probably due to the turbulent mixing dominating the molecular diffusion.

The compound angle injection leads to an asymmetric counter-rotating vortex pair which is observed in the mean vorticity field. The CVP is dominated by one vortex and the other vanishes quickly after the injection. The stronger vortex is highly responsible for the shape of the jet in the far field.

The entrainment of the present jet is compared with a symmetric jet by Bodart et al. [4] which is without compound angle. The present asymmetric jet entrains always better, especially near the jet exit hole which seems to be due to the larger interface region between the jet and the crossflow. The difference in the jet cross section areas is greater than for the entrainment and therefore the mean velocity through the section is lower for the asymmetric jet. Consequently, the asymmetric jet is spread closer to the wall which is a desired feature for a film cooling configuration.

The evolution of the turbulent scalar flux was studied by analysing its transport equations. Each term appearing in the equation was evaluated and several conclu-

sions arise:

- The dissipation term is significantly lower than the other terms.
- The production term approximately balances the pressure scrambling term.
- The shape of the production term is close to the shape of the turbulent scalar flux.
- The production subterm interacting with the mean shear is responsible for the counter-gradient diffusion in the streamwise direction.

Some of the most commonly employed algebraic turbulent scalar flux models used in RANS computations were compared with the present LES results. The performance in the spanwise and wall normal directions was approximately similar. In the streamwise direction both extensions of the generalized gradient diffusion hypothesis (GGDH) improve the accuracy at the counter-gradient diffusion region in comparison to the initial one.

BIBLIOGRAPHY

[1] K. Abe and K. Suga, "Towards the development of a Reynolds-averaged algebraic turbulent scalar-flux model," *International Journal of Heat and Fluid Flow*, vol. 22, no. 1, pp. 19–29, 2001.

[2] J. Andreopoulos and W. Rodi, "Experimental investigation of jets in cross-flow," *Journal of Fluid Mechanics*, no. 138, pp. 93–127, 1984.

[3] C. Béguier and L. Fulachier, "The turbulent mixing layer with an asymmetrical distribution of temperature," *Journal of Fluid Mechanics*, vol. 89, pp. 561–587, 1978.

[4] J. Bodart, F. Coletti, I. Bermejo-Moreno, and J. Eaton, "High-fidelity simulation of a turbulent inclined jet in a crossflow," *Center for Turbulence Research Annual Research Briefs*, pp. 263–275, 2013.

[5] D. G. Bogard, *The Gas Turbine Handbook*. National Energy Technology Laboratory, 2006, ch. 4.2.2.1 Airfoil Film Cooling.

[6] C. H. Bosanquet and J. L. Pearson, "The spread of smoke and gases from chimneys," *Transactions of the Faraday Society*, vol. 32, p. 1249, 1936.

[7] C. J. Chien and J. A. Schetz, "Numerical Solution of the Three-Dimensional Navier-Stokes Equations with Application to Channel Flows and a Buoyant Jet in a Cross-Flow," *Journal of Applied Mechanics*, vol. 42, pp. 575–579, 1975.

[8] F. Coletti, M. J. Benson, J. Ling, C. Elkins, and J. K. Eaton, "Turbulent transport in an inclined jet in crossflow," *International Journal of Heat and Fluid Flow*, vol. 43, pp. 149–160, 2013.

[9] B. J. Daly and F. H. Harlow, "Transport Equations in Turbulence," *Physics of Fluids*, vol. 13, no. 11, pp. 2634–2649, 1970.

[10] A. Favre, "Turbulence: space-time statistical properties and behavior in supersonic flows," *Physics of Fluids*, vol. 23, no. 19, pp. 2851–2863, 1983.

[11] T. F. Fric and M. Gharib, "Wake formation of the transverse jet," *Bulletin of the American Physical Society*, vol. 35, no. 2338, 1990.

[12] T. F. Fric and A. Roshko, "Vortical structure in the wake of a transverse jet," *Journal of Fluid Mechanics*, vol. 279, pp. 1–47, 1994.

[13] E. Garnier, N. Adams, and P. Sagaut, *Large Eddy Simulation for Compressible Flows*. Springer, 2009.

[14] R. J. Goldstein, E. R. G. Eckert, and J. W. Ramsey, "Film Cooling With Injection Through Holes: Adiabatic Wall Temperatures Downstream of a Circular Hole," *Journal of Engineering for Power*, pp. 384–393, 1968.

[15] R. J. Goldstein and J. R. Taylor, "Mass Transfer in the Neighborhood of Jets Entering a Crossflow," *Journal of Heat Transfer*, vol. 104, pp. 715–721, 1982.

[16] J. C. R. Hunt, A. Wray, and P. Moin, "Eddies, Streams, and Convergence Zones in Turbulent Flows," *Center for Turbulence Research Report*, pp. 193–208, 1988.

[17] I. S. Jung and J. S. Lee, "Effects of Orientation Angles on Film Cooling Over a Flat Plate: Boundary Layer Temperature Distributions and Adiabatic Film Cooling Effectiveness," *Journal of Turbomachinery*, vol. 122, pp. 153–160, 2000.

[18] Y. Kamotani and I. Greber, "Experiments on a turbulent jet in a cross flow," *AIAA Journal*, vol. 10, pp. 1425–1429, 1972.

[19] A. Kolmogorov, "Dissipation of energy in locally isotropic turbulence," *Dokl. Akad. Nauk SSSR*, vol. 32, 1941.

[20] A. Kolmogorov, "The local structure of turbulence in incompressible viscous fluid for very large Reynolds numbers," *Dokl. Akad. Nauk SSSR*, vol. 30, 1941.

[21] D. M. Kuzo, "An experimental study of the turbulent transverse jet," Ph.D. dissertation, California Institute of Technology, 1996.

[22] B. E. Launder, "On the computation of convective heat transfer in complex turbulent flows," *Journal of Heat Transfer*, vol. 110, pp. 1112–1128, 1988.

[23] K. Mahesh, "The Interaction of Jets with Crossflow," *Annual Review of Fluid Mechanics*, vol. 45, no. 1, pp. 379–407, 2013.

[24] K. T. McGovern and J. H. Leylek, "A Detailed Analysis of Film Cooling Physics: Part II - Compound-Angle Injection With Cylindrical Holes," *Journal of Turbomachinery*, vol. 122, pp. 113–121, 2000.

[25] S. Muppidi and K. Mahesh, "Two-dimensional model problem to explain counter-rotationg vortex pair formation in a transverse jet," *Physics of Fluids*, vol. 18, no. 8, 2006.

[26] S. Muppidi and K. Mahesh, "Direct numerical simulation of passive scalar transport in transverse jets," *Journal of Fluid Mechanics*, vol. 598, pp. 335–360, 2008.

[27] M. R. Overholt and S. B. Pope, "Direct numerical simulation of a passive scalar with imposed mean gradient in isotropic turbulence," *Physics of Fluids*, vol. 8, no. 11, pp. 3128–3148, 1996.

[28] S. B. Pope, *Turbulent flows*. Cambridge Univ Press, 2000.

[29] J. W. Ramsey and R. J. Goldstein, "Interaction of a Heated Jet With a Deflecting Stream," *Journal of Heat Transfer*, vol. 93, no. 4, pp. 365–372, 1971.

[30] O. Reynolds, "On the Dynamical Theory of Incompressible Viscous Fluids and the Determination of the Criterion," *The Royal Society*, pp. 123–161, 1894.

[31] L. F. Richardson, *Weather Prediction by Numerical Process*. Cambridge University Press, 1922.

[32] F. P. Ricou and D. B. Spalding, "Measurements of entrainment by axisymmetrical turbulent jets," *Journal of Fluid Mechanics*, vol. 11, pp. 21–32, 1961.

[33] M. M. Rogers, N. N. Mansour, and W. C. Reynolds, "An algebraic model for the turbulent flux of a passive scalar," *Journal of Fluid Mechanics*, vol. 203, pp. 77–101, 1989.

[34] K. Ryan, J. Bodart, M. Folkersma, C. J. Elkins, and J. Eaton, "Turbulent scalar mixing in a skewed jet in crossflow: experiments and modeling," in *TSFP9 conference*, 2015.

[35] J. Smagorinsky, "General circulation experiments with the primitive equations," *Monthly Weather Review*, vol. 91, no. 3, pp. 99–164, 1963.

[36] S. H. Smith and M. G. Mungal, "Mixing, structure and scaling of the jet in crossflow," *Journal of Fluid Mechanics*, vol. 357, pp. 83–122, 1998.

[37] K. A. Thole, A. K. Sinha, D. G. Bogard, and M. E. Crawford, "Mean Temperature Measurements of Jets with a Crossflow for Gas Turbine Film Cooling Application," in *Rotating Machinery Transport Phenomena*, 1990, pp. 69–85.

[38] E. Touber and N. D. Sandham, "Large-eddy simulation of low-frequency unsteadiness in a turbulent shock-induced separation bubble," *Theoretical and Computational Fluid Dynamics*, no. 23, pp. 79–107, 2009.

[39] S. Veeravalli and Z. Warhaft, "Thermal dispersion from a line source in the shearless turbulence mixing layer," *Journal of Fluid Mechanics*, vol. 216, pp. 35–70, 1990.

[40] A. W. Vreman, "An eddy-viscosity subgrid-scale model for turbulent shear flow: Algebraic theory and applications," *Physics of Fluids*, vol. 16, no. 10, pp. 3670–3681, 2004.

[41] Wikipedia. (2009) A schematic of a high-pressure turbine blade as used in aircraft engines. [Online]. Available: http://commons.wikimedia.org/wiki/File:GaTurbineBlade.svg

[42] P. T. Wooler, "Development of an Analytical Model for the Flow of a Jet into a Subsonic Crosswind," *NASA SP-218*, vol. September, pp. 101–119, 1969.

[43] Z.-T. Xie and I. P. Castro, "Efficient Generation of Inflow Conditions for Large Eddy Simulation of Street-Scale Flows," *Flow, Turbulence and Combustion*, vol. 81, no. 3, pp. 449–470, 2008.

[44] L. L. Yuan and R. L. Street, "Trajectory and entrainment of a round jet in crossflow," *Physics of Fluids*, vol. 10, pp. 2323–2335, 1998.

[45] C. H. N. Yuen and R. F. Martinez-Botas, "Film cooling characteristics of a single round hole at various streamwise angles in a crossflow: Part I effectiveness," *International Journal of Heat and Mass Transfer*, vol. 48, pp. 4995–5016, 2005.

[46] J. Ziefle and L. Kleiser, "Assessment of a film-cooling flow structure by large-eddy simulation," *Journal of Turbulence*, vol. 9, no. 29, pp. 1–25, 2008.

APPENDIX A. COMPUTATIONAL ASPECTS

The computations were carried on a French national super computer EOS in Toulouse operated by Calmip. The computer contains 612 nodes and each node contains 20 cores which is altogether 12 240 cores. Each node has 64 gigabytes (GB) of Random-access memory (RAM) which is altogether 39 terabytes (TB) of RAM. The performance is 274×10^9 floating-point operations per second (FLOPS).

The parallel scalability of Charles^X solver on EOS was measured by running four strong scaling tests. In the strong scaling tests the computational mesh size is kept constant while the number of cores is increased. Ideally, the speedup is proportional to the number of cores but in reality the increased communicational expense between the nodes and cores decreases the performance. The four strong scaling tests were done by using two mesh sizes with 80 and 160 million cells and two Message Passing Libraries (MPI), namely Intel MPI and Bullx MPI. Each test is begun by using the minimum number of nodes in terms of RAM which was for the smaller mesh 9 nodes and for the bigger mesh 18 nodes. The number of nodes was doubled between each simulation until the full capacity was reached.

Figure A.1 shows the results of the scaling tests. The scalability in plane (a) shows that the Intel MPI (solid and dash line) scales nearly linearly until 5 760 cores and then bends slightly down with both mesh sizes. The scalability is still 88 % and 78 % from the linear scalability respectively for the bigger mesh and smaller mesh. For the Bullx MPI with bigger mesh (point line) the scalability is almost always linear. However, interestingly, the performance with the smaller mesh (dot dash line) is worse with the small number of cores from 180 to 2880 than with the big number of cores above 2 880. This is probably due the nearly full memory usage which leads to lower performance.

The efficiency in plane (b) is measured by normalizing the wall time spent per iteration with (number of cells)/(number of cores). For both MPI's with bigger mesh (solid and point line) the efficiency is nearly identical until 5760 cores but Bullx MPI performs better with the maximum number of cores 11 520. The smaller mesh size shows more dramatic difference (dash and dot dashed lines). Bullx MPI performance is 20-30 % worse than Intel MPI performance with 180-1440 cores. After 1440 cores, the performance of Bullx MPI improves and with 11 520 cores Bullx MPI performs better than Intel MPI. The number of cells per core is for bigger mesh 13 889 and for the smaller mesh only 6 944. Therefore as a summary of the scaling tests the scalability of Charles^X is excellent on EOS. Bullx MPI outperforms Intel MPI with

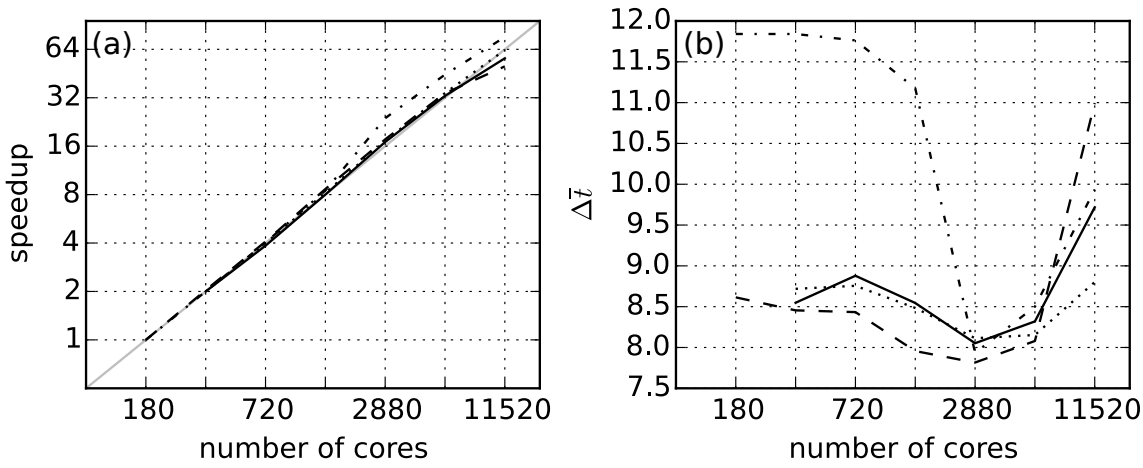

Figure A.1 *Scalability of Charles^X on EOS. (a) Speedup versus number of cores and (b) performance comparison between two MPI libraries. (solid line) Intel MPI with 160 million cells, (dash line) Intel MPI with 80 million cells, (point line) Bullx MPI with 160 million cells, (point dash line) Bullx MPI with 80 million cells and (grey line) linear scalability. $\Delta\bar{t}$ is time per iteration normalized with (number of cells)/(number of cores).*

the maximum number of cores but Intel MPI is better with the lower number of cores.

The present simulation was carried out by using 11 520 cores. The simulation was run for 40 hours of wall time in total, resulting almost 500 000 hours of central processing unit (CPU) time. During the simulation, a database is created by writing instantaneous and statistical data files. Altogether, 1032 instantaneous files and 53 statistical files are generated. Each instantaneous file is 13 GB in size and statistical file is 42 GB in size which makes the total output over 15.6 TB.